Manuscript title

Imprint of the Pacific Walker Circulation in global precipitation $\delta^{18}O$

Author List

Georgina Falster[1]

Bronwen Konecky[1]

Midhun Madhavan[2,3]

Samantha Stevenson[2]

Sloan Coats[4]

Author Affiliations

[1]Department of Earth and Planetary Sciences, Washington University in St. Louis, Missouri, USA

[2]Bren School of Environmental Science and Management, University of California, Santa Barbara, USA

[3]Department of Earth and Environmental Sciences, University of Michigan, Ann Arbor, USA

[4]Department of Earth Sciences, University of Hawaii-Manoa, Honolulu, USA

Corresponding Author

Georgina Falster (gfalster@wustl.edu)

Abstract

Characterising variability in the global water cycle is fundamental to predicting impacts of future climate change; understanding the role of the Pacific Walker circulation (PWC) in the regional expression of global water cycle changes is critical to understanding this variability. Water isotopes are ideal tracers of the role of the PWC in global water cycling, because they retain information about circulation-dependent processes including moisture source, transport, and delivery. We collated publicly-available measurements of precipitation $\delta^{18}O$ ($\delta^{18}O_P$), and used novel data processing techniques to synthesise long (34-year), globally-distributed composite records from temporally discontinuous $\delta^{18}O_P$ measurements. We investigated relationships between global-scale $\delta^{18}O_P$ variability and PWC strength, as well as other possible drivers of global $\delta^{18}O_P$ variability—including the El Niño Southern Oscillation (ENSO) and global mean temperature—and used isotope-enabled climate model simulations to assess potential biases arising from uneven geographical distribution of the observations or our data processing methodology. Co-variability underlying the $\delta^{18}O_P$ composites is more strongly correlated with the PWC ($r = 0.74$) than any other index of climate variability tested. We propose that the PWC imprint in global $\delta^{18}O_P$ arises from multiple complementary processes, including PWC-related changes in moisture source and transport length, and a PWC- or ENSO-driven ‘amount effect’ in tropical regions. The clear PWC imprint in global $\delta^{18}O_P$ implies a strong PWC influence on the regional expression of global water cycle variability on interannual to decadal timescales, and hence that uncertainty in the future state of the PWC translates to uncertainties in future changes in the global water cycle.

Significance statement

Anthropogenically-driven climate change has repercussions beyond global warming. One of the most impactful changes is to the global water cycle, but future changes to regional precipitation patterns on land are not well constrained. The Pacific Walker circulation (PWC) affects weather and climate far beyond the Pacific Ocean, and thus likely plays a role in global-scale precipitation patterns. But traditional approaches for assessing the PWC’s role in the global water cycle do not capture the full range of circulation-dependent processes including variability in moisture source, transport, and delivery. Here, we used water isotopes as a novel water cycle tracer, and found a strong PWC imprint in global water isotope patterns.

1 Introduction

As climate change progresses, many societally relevant impacts will be hydrological (e.g. drought and floods); these impacts are strongly linked with the global water cycle. Measures of the ‘global water cycle’ evaluated in terms of ratios of global-mean or zonally averaged precipitation relative to evaporation have shown that the global water cycle has intensified in past decades, in response to global warming (Huntington 2006; Durack et al. 2012; Cheng et al. 2020). This intensification follows the thermodynamical dependence of the atmospheric component of the globally-averaged water cycle on global temperature (Held and Soden 2006; Del Genio et al. 1991), and the trend is expected to continue with future warming (Allen and Ingram 2002; Meehl et al. 2000; Stephens and Hu 2010; O’Gorman 2015; Chou and Lan 2012; Greve et al. 2014). However, the spatial pattern of regional precipitation changes associated with an enhanced global water cycle is less well understood, due to the relative complexity of the changes, and the importance of associated shifts in atmospheric circulation (Vecchi and Soden 2007; Pfahl et al. 2017; Allan et al. 2020; Held and Soden 2006; Norris et al. 2019). Additionally, the zonal-mean approach commonly used to characterise the global water cycle masks the impacts of atmosphere-ocean dynamical processes—including the Pacific Walker circulation (PWC)—that drive geographic variability in the response of the global water cycle to global temperature change.

The PWC—the zonal component of atmospheric circulation over the equatorial Pacific Ocean—is an important driver of regional water cycle variability (Deser and Wallace 1990; Held and Soden 2006; DiNezio et al. 2010; Vecchi et al. 2006). The PWC can be characterised by a zonal sea level pressure (SLP) gradient across the equatorial Pacific, with deep convection over the Indo-Pacific Warm Pool (low SLP), westerlies in the upper troposphere, subsidence and radiative cooling over the equatorial eastern Pacific (high SLP), and surface easterlies (the Pacific trade winds) (Bjerknes 1969). On interannual time scales, the PWC is tightly coupled with equatorial Pacific sea surface temperature (SST) anomalies (Walker and Bliss 1932, 1937; Alexander et al. 2002) via the El Niño Southern Oscillation (ENSO), which is the dominant mode of interannual global climate variability.

Changes in the intensity of the PWC have known global consequences: for example, a strengthened PWC contributed to the decreased rate of global warming in the early 2000s (England et al. 2014; Kosaka and Xie 2013; Watanabe et al. 2014; Dai et al. 2015; Dong and McPhaden 2017). In the context of ENSO, the PWC also has known impacts on regional precipitation in the tropics (Soden 2000; Han et al. 2020) and beyond (e.g. Ropelewski and Halpert 1996; Domeisen et al. 2019; Ropelewski and Halpert 1987, 1989; Cole and Cook 1998; Dai et al. 1998; Kong and Chiang 2020), but uncertainties remain in the magnitude and geographic distribution of its impact (Seager et al. 2010), particularly on interannual to decadal time scales. This is in part because the combined local and remote PWC influence on atmospheric circulation has been difficult to evaluate with networks of *in situ* observations. Dynamically-driven changes in the global water cycle (e.g. regional circulation changes) are not well captured by commonly-used metrics such as precipitation and/or evaporation (Schneider et al. 2017; Trenberth et al. 2007; Schlosser and Houser 2007; Dagan et al. 2019), or related variables such as freshwater runoff (Dai et al. 2009), ocean salinity (Skliris et al. 2016; Yu et al. 2020), atmospheric moisture content (Dai et al. 2011), or combinations of these water cycle components (Huntington 2006; Zhang et al. 2019).

The oxygen stable isotopic composition of precipitation (the ratio of ^{18}O to ^{16}O in precipitation relative to the ratio of ^{18}O to ^{16}O in a standard reference material; $\delta^{18}O_P$) is an ideal tool for characterising circulation changes, including those associated with the PWC. Precipitation with lower δ^{18}O has less of the heavy isotope (^{18}O); precipitation with higher δ^{18}O has relatively more ^{18}O. Water phase changes (such as evaporation and condensation) are mass-dependent, and result in isotopic fractionation; water molecules containing an ^{18}O condense more readily than isotopologues with only ^{16}O. Conversely, isotopologues with only ^{16}O evaporate more readily than those with the heavier isotope. For example, when liquid water evaporates, the evaporate is depleted in ^{18}O relative to the liquid water's initial isotopic composition (i.e. the vapour will have lower δ^{18}O); accordingly, due to the relatively high loss of ^{16}O, the remaining liquid becomes enriched in ^{18}O (i.e. the remaining liquid will have higher δ^{18}O). The δ^{18}O of both phases depends both on the initial isotopic composition of the water, and also environmental factors such as ambient temperature and relative humidity, which influence the amount of fractionation. Water phase changes are therefore associated with a change in that water's $^{18}O/^{16}O$, such that $\delta^{18}O_P$ can retain information about atmospheric processes operating at scales from individual hydrometeors to large-scale circulation systems (Konecky et al. 2019; Bowen et al. 2019; Galewsky et al. 2016).

Recent studies have identified distinct $\delta^{18}O_P$ signatures of individual atmospheric processes that the PWC is known to affect, but which cannot be easily characterised by observations of precipitation amount and/or evaporation. For example, the proportion of convective versus stratiform rainfall (Aggarwal et al. 2016; Araguás-Araguás et al. 2000), below-cloud processes (Graf et al. 2019), and changing moisture source and transport pathways (Nusbaumer and Noone 2018) can each influence $\delta^{18}O_P$, depending on local and regional climate. In some parts of the tropics, $\delta^{18}O_P$ is negatively correlated with precipitation amount (Conroy et al. 2016; Konecky et al. 2019; Kurita 2013; Dansgaard 1964; Rozanski et al. 1993). This simple empirical relationship—the observed negative correlation of precipitation amount with $\delta^{18}O_P$ in tropical climates—is known as the 'amount effect', and is the result of many atmospheric processes (Konecky et al. 2019) including convective intensity (Risi et al. 2010; Samuels-Crow et al. 2014; Cai and Tian 2016a; Stewart 1975; Dee et al. 2018), changes in vapour convergence (Moore et al. 2014), and upstream rainfall and convection (Kurita et al. 2009; Zwart et al. 2016). Each of these atmospheric processes is known to be influenced by the PWC, in its role as the atmospheric arm of ENSO (e.g. Soden 2000; Han et al. 2020; Ropelewski and Halpert 1989, 1996). Although $\delta^{18}O_P$ measurements integrate information from many individual processes and circulation features, these measurements have yet to be leveraged to evaluate the holistic imprint of the PWC in the global water cycle.

$\delta^{18}O$ has been measured in precipitation since the 1950s, and tens of thousands of $\delta^{18}O_P$ measurements are freely available from the Global Network of Isotopes in Precipitation database (GNIP) (IAEA/WMO 2020) and other online repositories (e.g. Bowen et al. 2019; Putman and Bowen 2019). But the spatial coverage of $\delta^{18}O_P$ datasets is patchy, and temporal coverage is irregular and often discontinuous even at individual sites. The shorter records comprising most published $\delta^{18}O_P$ data have no long common time period of overlap, precluding characterisation of temporal $\delta^{18}O_P$ variability at a global scale. Previous global-scale $\delta^{18}O_P$ meta-analyses have therefore focused on static spatial $\delta^{18}O_P$ patterns (Bowen and Wilkinson 2002; Bowen 2008; Terzer et al. 2013) or climatological distributions of isotopes in precipitation and vapour (Araguás-Araguás et al. 2000), or relied on the outputs of isotope-enabled climate models, calibrated against $\delta^{18}O_P$ climatologies from observations (Brown et al. 2006; Nusbaumer et al. 2017), with two recent exceptions examining site-level decadal trends in $\delta^{18}O_P$ (Putman et al. 2021; Vystavna et al. 2020).

Here we assess the magnitude and spatial extent of the PWC imprint in observations of global $\delta^{18}O_P$. To maximise information from temporally and spatially discontinuous $\delta^{18}O_P$ records, we employed a 'dynamic compositing' technique (Section 2.8.1) that had not previously been applied to globally-distributed $\delta^{18}O_P$ observations. We then evaluated the relationship of global

$\delta^{18}O_P$ with the PWC, as well as other modes of climatic variability. To assess potential biases arising from inconsistent spatio-temporal data coverage, we repeated several analyses using global $\delta^{18}O_P$ simulated by the isotope-enabled Community Earth System Model Last Millennium Ensemble (iCESM iLME; Brady et al. 2019; Stevenson et al. 2019).

Specifically, Section 3.1 describes site-level correlations of $\delta^{18}O_P$ with the PWC and other climate indices. Section 3.2 describes static global $\delta^{18}O_P$ anomalies associated with anomalously strong or weak PWC years (analogous to La Niña and El Niño events), in observations and the iLME. Section 3.3 describes spatio-temporal variability in global $\delta^{18}O_P$, in observations and the iLME. Sections 4 and 5 summarise the relationship between global $\delta^{18}O_P$ and the PWC, and discuss implications for regional variability within the global water cycle.

2 Data and methods

2.1 Precipitation $\delta^{18}O$ data

We used monthly water isotope measurements available from GNIP (IAEA/WMO 2020), supplemented by published $\delta^{18}O_P$ datasets available from http://waterisotopes.org (the 'Water Isotopes Database'; wiDB), with sub-monthly data converted to monthly means where necessary, following Putman et al. (2019). We downloaded all monthly data available from GNIP in March 2020, and all $\delta^{18}O_P$ data from the wiDB in August 2020. The databases contain measurements of both the oxygen and hydrogen stable isotopic composition of water. We use only $\delta^{18}O_P$, as it has greater spatial and temporal coverage. We also obtained data from 15 stations in Australia from the Australian Nuclear Science and Technology Organisation (ANSTO) (Hollins et al. 2018) (Fig. 1 & Supp. Fig. 1). $\delta^{18}O_P$ values in all databases are provided in per mille relative to Vienna Standard Mean Ocean Water (VSMOW).

We removed redundant records for sites in multiple databases, preferentially keeping the GNIP data because for most such datasets, these are the original versions. We also filtered out sites with fewer than two consecutive years of monthly measurements, resulting in a total of 959 sites (Fig. 1). For analyses reliant on calculation of anomalies and/or where we used annually-averaged data, we further filtered this dataset to only include the 307 sites with five or more years of monthly measurements (Supp. Fig. 1). In both cases, stations are biased to the Northern Hemisphere mid-latitudes (Fig. 1 & Supp. Fig. 1).

2.2 Observational and climate reanalysis data

We used gridded monthly-mean observational and reanalysis datasets to investigate the relationship of $\delta^{18}O_P$ values with atmospheric and oceanic climate variables. Although GNIP and ANSTO station data include concurrent precipitation amount observations, datasets available from the wiDB do not. For terrestrial precipitation, we therefore used the 1° monthly gridded precipitation product from the Global Precipitation Climatology Centre (GPCC) (Becker et al. 2013). The GPCC grid spans 1891 to 2016, and is derived from rain gauge measurements at over 116,000 stations. To maintain consistency, we used GPCC for all calculations requiring precipitation amount information; the precipitation data in the GNIP/ANSTO datasets and GPCC are mostly similar (Supp. Fig. 2). For calculation of amount-weighted annual-mean $\delta^{18}O_P$, we used the GPCC grid point closest to each water isotope observation station. For $\delta^{18}O_P$ records extending past 2016, we used the monthly precipitation amount measurements available in the GNIP/ANSTO datasets. To visualise precipitation patterns over the oceans, we used the shorter (1979 to present) Climate Prediction Centre (CPC) merged analysis of precipitation product (CMAP), which is derived from satellite and rain gauge observations and therefore has global coverage (Xie and Arkin 1997) .

Historical sea level pressure (SLP) data is from the Hadley Centre Sea Level Pressure dataset (HadSLP2r), available at 5° resolution spanning 1850 to present (Allan and Ansell 2006). Historical sea surface temperature (SST) data is from the NOAA Extended Reconstructed Sea Surface Temperature V5 (ERSSTv5) dataset, which spans 1854 to present, on a 2° grid (Huang et al. 2017). Historical land surface temperature (LST) data is from the Berkeley Earth surface temperature dataset, available at 1° resolution spanning 1850 to present (Rohde and Hausfather 2020). We obtained the zonal (u) and meridional (v) wind fields at 200, 850, and 1000 hPa from the ERA5 reanalysis (Copernicus Climate Change Service (C3S) 2017). At the time we performed our analyses, monthly observations were available at 0.25° resolution, spanning 1979 to 2018. To compare the ERA5 surface wind field with observations, we also obtained the u and v components of 10 m wind from the Wave and Anemometer-based Sea Surface Wind (WASWind) dataset, which spans 1950 to 2009, on a 4° grid (Tokinaga 2012).

2.3 Climate model data

We investigated the relationship between $\delta^{18}O_P$ and various other climate variables in the isotope-enabled Last Millennium Ensemble (iLME; Stevenson et al. 2019; Brady et al. 2019). The iLME is a set of eight fully coupled simulations run using the isotope-enabled Community

Earth System Model version 1 (iCESM; Brady et al. 2019), which tracks water isotopologues and their fractionation through the climate system. Simulations extend from 850 to 2005 CE at a nominal horizontal resolution of 1° (ocean) or 2° (atmosphere/land), and include either all anthropogenic and natural external forcing factors ('full-forcing' simulations), or only one external forcing factor ('single-forcing' simulations). In this paper we only use the three full-forcing simulations, as they provide the most direct comparison with observations. $\delta^{18}O_P$ simulated by iCESM generally compares well with $\delta^{18}O_P$ from the GNIP (Brady et al. 2019; Nusbaumer et al. 2017).

2.4 Climate indices

2.4.1 Indices for the strength of the PWC

We calculated a PWC index using data from HadSLP2r, based on the SLP gradient along the equatorial Pacific Ocean, (Vecchi et al. 2006). The SLP gradient is defined as the difference between the area-mean SLP anomalies over the central-eastern Pacific Ocean (160°W-180°W, 5°S-5°N) and the western Pacific/eastern Indian oceans (80°E-160°E, 5°S-5°N). This gradient is related to the strength of the PWC (Vecchi et al. 2006), particularly as a reliable proxy for the intensity of equatorial Pacific zonal winds (Clarke and Lebedev 1996), and has been used in many other studies of the PWC (e.g. Chung et al. 2019; Kang et al. 2020; Misios et al. 2019; DiNezio et al. 2013; Hou et al. 2018; Yim et al. 2017; Tian and Jiang 2020). The ΔSLP *index* is the anomaly in the SLP gradient relative to the monthly climatology for 1960-2019. Positive (negative) ΔSLP values represent an increased (decreased) zonal pressure gradient, and hence stronger (weaker) PWC.

We tested the sensitivity of our analyses to our choice of ΔSLP as a PWC proxy by repeating several analyses using two other indices for equatorial Pacific atmospheric variability: 1) the Southern Oscillation Index (SOI), and 2) PWC_{uwinds}, an index based on surface zonal winds above the equatorial Pacific Ocean (Chung et al. 2019). The SOI is the standardised anomaly of the SLP difference between Tahiti and Darwin (Troup 1965). The PWC_{uwinds} index is the surface zonal wind anomaly at 180°W-150°W, 6°S-6°N, where positive (negative) values represent anomalously westerly (easterly) winds, and hence weaker (stronger) PWC (Chung et al. 2019). We calculated the PWC_{uwinds} index using both WASWind and the 1000 hPa (nearest surface) zonal wind field from ERA5; in the interval of overlap the two indices are very similar, in terms of interannual variability and trends (not shown). We therefore used the longer ERA5-based

PWC_{uwinds} index. All three PWC indices (ΔSLP, SOI, PWC_{uwinds}) are highly correlated (Supp. Fig. 3).

2.4.2 Other climate indices

We used the Niño 3.4 and ENSO Modoki indices to investigate the influence of oceanic conditions (ENSO) as opposed to atmospheric processes on global $\delta^{18}O_P$ values. The Niño 3.4 index is the SST anomaly in the central equatorial Pacific Ocean (170°W-120°W, 5°S-5°N). The ENSO Modoki index is based on SST anomalies in three boxes in the Pacific Ocean, and is more sensitive to central Pacific El Niño events than the Niño 3.4 index (Ashok et al. 2007). We used both indices because SST anomalies associated with ENSO events may be centred in different parts of the Pacific (central versus eastern Pacific), and these different centres of action incite different atmospheric responses. By considering both indices we account for at least some of the potential influence of ENSO diversity on global $\delta^{18}O_P$ patterns. To investigate the possible influence of extra-Pacific and extra-tropical climate modes on global $\delta^{18}O_P$ values, we also use the Indian Ocean Dipole (the Dipole Mode Index, DMI, as calculated by NOAA), the Southern Annular Mode (SAM, as calculated by NOAA), and the Pacific Meridional Mode (PMM; Chiang and Vimont 2004), as well as global mean surface temperature (GMST; Lenssen et al. 2019; GISTEMP Team 2020).

2.5 Calculating annual mean values from monthly data

For all analyses using annually-averaged values, we report results in 'tropical years', where each year starts in May of calendar year 1 and finishes in April of calendar year 2. For example, the tropical year starting in May 1991 and finishing in April 1992 is designated tropical year 1991. This allows for use of annual averages while still capturing the growth, peak, and decay of El Niño/La Niña events, which are relevant to the PWC on interannual time scales. To calculate precipitation-weighted annual mean $\delta^{18}O_P$ values, monthly precipitation $\delta^{18}O_P$ values were weighted by that month's precipitation amount (from the nearest GPCC grid point) before calculating annual mean $\delta^{18}O_P$.

2.6 Determining site-level relationships of $\delta^{18}O_P$ and precipitation with climate modes

We computed the Pearson correlation coefficient for precipitation-weighted annual mean $\delta^{18}O_P$ with annual mean ΔSLP, at individual stations. For this analysis, we used all stations with five or more years of continuous data (Supp. Fig. 1). We performed the same analysis on the GPCC precipitation field (starting in 1960 to match the $\delta^{18}O_P$ data), as well as GPCC data downsampled to exactly match the spatial and temporal coverage of the $\delta^{18}O_P$ data (for easier visual comparison). To test the sensitivity of the correlation patterns to interannual versus sub-annual variability, we repeated this analysis, but for each site calculating the correlation of monthly (as opposed to annual) ΔSLP with monthly $\delta^{18}O_P$ anomalies at all stations with two or more years of continuous data.

2.7 Spatial $\delta^{18}O_P$ anomalies associated with strong and weak PWC years

2.7.1 Spatial $\delta^{18}O_P$ anomalies in observational data

We created anomaly maps for years in which the PWC was anomalously strong or weak, to determine whether there is a distinct $\delta^{18}O_P$ spatial fingerprint for ΔSLP anomalies, as has been observed with other climate modes (Vuille and Werner 2005; Vuille et al. 2005; Cai et al. 2017), and for ENSO-related atmospheric water vapour stable isotopic anomalies (Dee et al. 2018; Sutanto et al. 2015). We defined events similarly to the NOAA operational El Niño and La Niña event definition: anomalous years (in tropical years as defined in Section 2.5) are those in which a three-month moving average of monthly ΔSLP exceeds one standard deviation from the 1960-2019 mean, for five or more consecutive months. For all $\delta^{18}O_P$ stations with five or more years of continuous data, we calculated amount-weighted annual means, and then calculated annual anomalies relative to the site long-term mean. For each strong or weak PWC year, we show anomalies for sites that have data in that year. For comparison, we also calculated the SST anomalies in the same years.

2.7.2 Spatial $\delta^{18}O_P$ anomalies in iCESM data

We replicated the analysis described in Section 2.7.1 using $\delta^{18}O_P$ data from the three iLME full-forcing simulations. We determined 'strong' and 'weak' PWC years exactly as in Section 2.7.1, starting in model year 1960. Given the complete spatial and temporal coverage of the model output, rather than show $\delta^{18}O_P$ anomaly maps for individual years as is necessary for the observational data, we calculated composite $\delta^{18}O_P$ anomalies for each case (one composite each for anomalously positive and negative ΔSLP). To highlight areas where the $\delta^{18}O_P$ anomaly is consistently of the same sign, we stippled grid cells where ≥90 % of years agree on the sign of the anomaly (i.e. whether $\delta^{18}O_P$ in that grid cell is consistently positive or negative relative to the long-term mean). We also masked areas where fewer than 66 % of grid cells agree on the direction of the $\delta^{18}O_P$ anomaly in each case. To visualise the corresponding atmospheric anomalies, we repeated this analysis using the iLME SLP fields.

2.8 Influences on interannual to decadal spatio-temporal variability in $\delta^{18}O_P$

2.8.1 Calculating composite $\delta^{18}O_P$ records

We are particularly interested in the spatio-temporal response of $\delta^{18}O_P$ to changes in the strength of the PWC on interannual to decadal time scales. But there is a limit to the information that can be gleaned from short records covering disparate time intervals (e.g. Fig. 1). We therefore adapted the ‘dynamic compositing’ method of Kaufman et al. (2020) and Falster et al. (2019)—developed for discontinuous palaeoclimate time series—to synthesise the global monthly $\delta^{18}O_P$ data into a smaller number of long, regional $\delta^{18}O_P$ composites. Dynamic compositing is an iterative compositing method that preserves the data structure within the composite (including trends, if any). Temporal chunks from each original time series are randomly selected and then used to adjust the $\delta^{18}O_P$ variance to match records in that composite that have data in the same time interval. The *mean* of each $\delta^{18}O_P$ timeseries is then iteratively adjusted to minimise the mean offset to all other records in the composites (again, that have data in the same time interval). Using this method, time series that only cover part of the full interval, or have no overlap with some other time series, are ‘slotted’ into the composite without causing spurious jumps. The method can therefore produce robust composite records, while including some time series that do not overlap. The compositing process is repeated many times (using different random chunks to dictate time series alignment) to produce composite ensembles where the median timeseries preserves both the trend and interannual variability.

To determine which station data should be composited together, we used k-means clustering (k = 50) to group stations based on geographic proximity, precipitation seasonality, and annual-mean $\delta^{18}O_P$. We quantified precipitation seasonality using the equation below, which measures how much the seasonal cycle of precipitation deviates from a uniform distribution:

$$precipitation\ seasonality = \frac{1}{MAP} \times \sum_{December}^{January} \left| Ppt_{Each\ Month} - \frac{MAP}{12} \right|$$

where $Ppt_{Each\ Month}$ refers to the mean precipitation amount in each month, and MAP is the mean annual precipitation at that site. We started with 50 clusters as this qualitatively balanced 1) separating stations with different climatic and geographic characteristics (e.g. relationship with regional topography, distance from the coast), and 2) retaining sufficient stations in each cluster to produce composite records with consistent temporal coverage. After performing the clustering, we manually checked each cluster for records in which the annual-mean $\delta^{18}O_P$ or geography was obviously dissimilar, and split clusters where necessary, resulting in 52 clusters. On average, sites within a cluster are 430 km from the cluster centroid. Using the dynamic compositing, for each cluster we calculated 50 composite monthly $\delta^{18}O_P$ records, and took the median of that ensemble. We then took the mean of all GPCC grid cells corresponding to the $\delta^{18}O_P$ stations in that cluster and calculated a single amount-weighted annual mean $\delta^{18}O_P$ record for each regional composite. We truncated the composite records to 1982-2015 inclusive (tropical years); this interval struck a balance between a sufficiently long time interval for investigating interannual to decadal variability, and retaining as many records as possible with good temporal coverage (described in more detail in the following section).

2.8.2 Global $\delta^{18}O_P$ principal components analysis

From a group of spatially dispersed records, the leading principal components (PCs) reflect information common to the records, relegating noise and site-specific climatic variability to subsequent PCs (Braganza et al. 2009). We therefore performed Principal Component Analysis (PCA) on a subset of the centred and scaled regional $\delta^{18}O_P$ composites. We used the data interpolation empirical orthogonal function (DINEOF) approach (Beckers et al. 2006), which allows robust computation of PCA on data with some missing values. Interpolation skill decreases with increasing number of missing values, so we first filtered the regional composite $\delta^{18}O_P$ records to retain only the 16 records (from the original 52) with temporal coverage greater than 80 %. The sign of a PC is arbitrary, so for clarity of interpretation we aligned PC1 to be positively correlated with ΔSLP. For comparison, we repeated this analysis using precipitation *amount*, downsampled to match the spatial coverage of the $\delta^{18}O_P$ data, i.e. from the GPCC grid cells closest to the locations of records contributing to each of the 16 regional composites.

We calculated correlations of the composite $\delta^{18}O_P$ and precipitation PC1s with ΔSLP. To test the robustness of the results to our choice of PWC index, we also calculated correlations with the SOI and PWC_{uwinds}. To examine the role of tropical Pacific oceanic variability, we assessed the relationship of the $\delta^{18}O_P$ and precipitation PC1s with the Niño 3.4 and ENSO Modoki indices. We used the DMI, the SAM index, the PMM index, and GMST to assess the possible influence of extra-Pacific and extra-tropical climate modes.

Finally, to determine the influence of *individual* regional composites on the relationship of the composite $\delta^{18}O_P$ PC1 with ΔSLP, we calculated PC1 of all possible subsets of the 16 regional composites i.e. using all possible combinations of two to 15 of the $\delta^{18}O_P$ composites. We then calculated the correlations of each of those composite $\delta^{18}O_P$ PC1s with ΔSLP.

2.9 Influences on interannual to decadal spatio-temporal variability in $\delta^{18}O_P$ in iCESM

To test 1) whether our results are biased by the dynamic compositing described in Section 2.8.1, 2) whether our results (interpreted in terms of the global water cycle) are biased by the locations of available observational data, and 3) if $\delta^{18}O_P$-PWC-climate relationships are similar in climate model simulations and observations, we performed our data handling steps and subsequent analyses on $\delta^{18}O_P$ data from the iLME. We report the mean results from the three full-forcing simulations.

The spatio-temporally complete nature of iCESM output allows us to use the simulated $\delta^{18}O_P$ fields to isolate the effects of sampling biases. Therefore, to test questions 1) and 2) above, we performed PCA on three $\delta^{18}O_P$ subsets from the iLME full-forcing simulations, each derived using a different subsampling method (described below). As the iLME simulations finish in calendar year 2005, we performed these analyses for 1971-2004 (tropical years). First, we calculated regional composites from iCESM data as described in Section 2.8.1 (including the dynamic compositing), using $\delta^{18}O_P$ from the grid cells corresponding to each station, subsampled to exactly the same temporal coverage as each component record; this is denoted the 'dynamic composite' subset. Second, for each cluster we took the mean of the grid cells corresponding to sites within that cluster (i.e. spatially but *not* temporally subsampled); this is denoted the 'cluster means' subset. Third, we simply used the single iLME grid cell closest to the cluster centroid of each regional composite; this is denoted the 'cluster centroids' subset. We also calculated PC1 of the full $\delta^{18}O_P$ field—to ensure equal area weighting, the gridded data were weighted by the square root of the cosine of latitude. This provides insight into whether site-level differences, temporal gappiness, or the compositing method cause artifacts in the regional composite $\delta^{18}O_P$ PC1, relative to the true global $\delta^{18}O_P$ PC1. We calculated ΔSLP as described in Section 2.4.1, using the iLME SLP data.

3 Results

3.1 Correlations of site-level $\delta^{18}O_P$ with ΔSLP

On the western side of the Pacific Ocean, site-level $\delta^{18}O_P$ in the tropics and subtropics is negatively correlated with ΔSLP, on both monthly and annual timescales (Fig. 2a & Supp. Fig. 4a); precipitation amount in the same areas is mostly positively correlated with ΔSLP, except some of eastern China (Fig. 2b & Supp. Fig. 4b). This negative $\delta^{18}O_P$/positive precipitation correlation pattern is also the case for the northern tip of South America. The opposite is broadly true for Japan, southern South America, and the Galápagos Islands (equatorial eastern Pacific).

In central to western North America, $\delta^{18}O_P$ is mostly negatively correlated with ΔSLP; in contrast to this, the precipitation correlations vary from negative in the subtropics to positive further north. Across Europe, correlations of local $\delta^{18}O_P$ with ΔSLP are more often positive than negative, although the spatial distribution of significant relationships is not particularly coherent. $\delta^{18}O_P$ and precipitation in most of the rest of North and South America, Greenland, Africa, and western Europe is not significantly correlated with ΔSLP on annual or monthly time scales. Correlations of precipitation with ΔSLP are generally weaker than those of $\delta^{18}O_P$ in the same locations.

3.2 Isotopic fingerprint of individual anomalously strong and weak PWC years

3.2.1 Isotopic fingerprint of strong and weak PWC in observational data

All six years with anomalously negative ΔSLP (weak PWC) coincide with El Niño events; five of the six years with anomalously positive ΔSLP (strong PWC) coincide with La Niña events (2013-2014 being the exception) (Fig. 3a). However, there is no consistent $\delta^{18}O_P$ spatial fingerprint associated with individual years of anomalously positive or negative ΔSLP (Supp. Fig. 5 & 6). This suggests that—as is the case for El Niño and La Niña events (Capotondi et al. 2015)—no two anomalously weak or strong PWC years have an identical impact on global hydroclimate. The influence of the PWC is transmitted from the tropical Pacific by a wide variety of teleconnections, many of which are influenced by other modes of climate variability (Alexander et al. 2002), as well as by long-term climate trends and stochastically driven internal atmospheric variability (Stevenson et al. 2015). Most anomalous PWC years overlap with El Niño or La Niña events, and global teleconnections—including the atmospheric bridge—during ENSO events are known to be both non-linear and non-stationary (Batehup et al. 2015; Coats et al. 2013).

3.2.2 Isotopic fingerprint of strong and weak PWC in iCESM

Similar to in observations, there is little consistency in the spatial $\delta^{18}O_P$ expression of individual anomalously positive or negative ΔSLP years in the iLME (Supp. Fig. 7a and 7b). This is particularly the case over land i.e. where observational data are collected; the signal over the Pacific Ocean is more coherent. Regarding terrestrial $\delta^{18}O_P$ specifically, anomalies over parts of India, China, and north-central Africa are consistently of the same sign (stippling in Supp. Fig. 7a and 7b). Such consistency suggests that PWC teleconnections to these regions during years of anomalous ΔSLP may be relatively stable, although this warrants further investigation. SLP anomalies are also relatively inconsistent outside the tropical Pacific Ocean, further suggesting that years of anomalously positive or negative ΔSLP are associated with non-stationary atmospheric teleconnections in the iCESM as well as in observations.

3.3 Spatio-temporal variability in $\delta^{18}O_P$

3.3.1 PCA performed on observational data

The leading principal component of the 16 regional $\delta^{18}O_P$ composites from *in situ* data (global $\delta^{18}O_P$ PC1) is strongly linearly correlated with ΔSLP ($r = 0.74$, $p < 0.05$) (Fig. 4, shown alongside the corresponding empirical orthogonal function, global $\delta^{18}O_P$ EOF1). Global $\delta^{18}O_P$ PC1 is more strongly correlated with the strength of the PWC (whether from ΔSLP, PWC_{uwinds}, or the SOI) than with any other index of climate variability, including SST-based ENSO metrics (Niño 3.4 and the El Niño-Modoki Index), and indices of variability outside the tropics (the PMM, the DMI, and the SAM) (Table 1). This demonstrates that on interannual to decadal timescales globally, $\delta^{18}O_P$ predominantly responds to atmospheric circulation in the tropical Pacific. Most regional $\delta^{18}O_P$ composites map negatively onto global $\delta^{18}O_P$ PC1 i.e. $\delta^{18}O_P$ decreases as ΔSLP increases (blue-coloured points in Fig. 4a); for the remainder of the composites, $\delta^{18}O_P$ increases as ΔSLP increases. This is largely consistent with the ΔSLP correlations with $\delta^{18}O_P$ at the individual sites contributing to the regional composites (Fig. 2a).

The correlation pattern of global $\delta^{18}O_P$ PC1 with surface temperature anomalies is similar to that of ΔSLP with surface temperature anomalies (Fig. 5b. compared with Fig. 3d), with significant correlations concentrated in the Pacific and Southern oceans. The main differences are a relatively strong positive correlation with SST in the mid- to north Atlantic Ocean, negative correlations with SST in the Southern Ocean south of Australia, and stronger correlations with LST across southern mainland Asia and northern Africa. The correlation pattern of global $\delta^{18}O_P$ PC1 with SLP anomalies is strongly reminiscent of the ΔSLP-SLP correlation pattern (Fig. 5a compared with Fig. 3b), particularly in the low-latitudes of the Indian and Pacific oceans. The correlation pattern of terrestrial precipitation amount with global $\delta^{18}O_P$ PC1 is virtually indistinguishable from that between ΔSLP and precipitation amount (Fig. 5c compared with Fig. 3b): an increase in global $\delta^{18}O_P$ PC1 is correlated with positive precipitation anomalies over Australia, the maritime continent, and north-western South America; and negative precipitation anomalies in south-western North America. Global $\delta^{18}O_P$ PC1 is also associated with negative precipitation anomalies over the central Pacific and western Indian oceans, and positive precipitation anomalies over the western Pacific, in the Pacific sector of the Southern Ocean, and the eastern Pacific just south of the equator.

Tropical locations where a negative loading in global $\delta^{18}O_P$ EOF1 (black circles in Fig. 5c) co-occurs with a positive correlation between precipitation amount and global $\delta^{18}O_P$ PC1 (and vice versa) likely reflect a PWC-driven amount effect—these being northern Australia, the maritime continent, and northern South America. Elsewhere—particularly in north America— the spatial loading pattern of global $\delta^{18}O_P$ EOF1 does not exactly follow the direction of precipitation anomalies, suggesting that the PWC imprint on $\delta^{18}O_P$ instead reflects changes in moisture source regions and atmospheric transport that affect $\delta^{18}O_P$ without necessarily producing local precipitation anomalies.

Upper-level and near-surface wind anomalies associated with global $\delta^{18}O_P$ PC1 show coherent circulation changes (Fig. 5d & 5e). An increase in global $\delta^{18}O_P$ PC1 is associated with strengthening of the trade winds over the Pacific Ocean and westerly anomalies in the northern Indian ocean, consistent with a strengthening of the PWC (Fig 5d). This is also evident in the 200 hPa wind anomalies, with strengthened westerlies aloft over the equatorial Pacific (Fig 5e). In both the upper and lower troposphere, an increase in global $\delta^{18}O_P$ PC1 is associated with zonally asymmetric strengthening of the westerly wind belt in the Southern Hemisphere, particularly in the Pacific sector of the Southern Ocean. The wind anomaly fields also show strengthened westerlies across the northern USA, and weakened flow across southern North America. Global $\delta^{18}O_P$ PC1 is not associated with robust circulation anomalies over most of northern Europe, northern Africa, and the North Atlantic, explaining the lack of coherent site-level $\delta^{18}O_P$-ΔSLP correlations in these regions (Fig. 2a).

3.3.2 Influence of individual $\delta^{18}O_P$ composites on the relationship between global $\delta^{18}O_P$ PC1 and ΔSLP

The median correlation of ΔSLP with PC1 from subsets of the 16 regional $\delta^{18}O_P$ composites decreases as fewer composites are included in the PCA (Supp. Fig. 8). However, the consistently high maximum correlations for each group of subsets (i.e., those containing the same number of composites) suggests that there are regions where $\delta^{18}O_P$ is particularly strongly correlated with ΔSLP; this is reflected in the global $\delta^{18}O_P$ EOF1, where sites close to the Pacific—particularly on the western rim—load particularly strongly onto global $\delta^{18}O_P$ PC1 (darkest blue points in Fig. 4a).

3.3.3 Effects of dynamic compositing and station distribution on PCA

The first PCs of $\delta^{18}O_P$ variability in the full iLME $\delta^{18}O_P$ field and the three iLME subsets—dynamic composites, cluster means, and cluster centroids—are similar (Fig. 6, Table 2). This suggests 1) that the compositing method used on the observational data does not strongly bias the results, and 2) that the 16 regional composites from the observational data capture a realistic approximation of spatio-temporal changes in *global* $\delta^{18}O_P$, at least as simulated by iCESM.

3.3.4 PCA performed on iLME $\delta^{18}O_P$ data

Giving confidence to results presented Sections 3.3.1 and 3.3.3, we see broadly similar $\delta^{18}O_P$-ΔSLP relationships in the iLME to the observations, with strong correlations between $\delta^{18}O_P$ PC1 and ΔSLP for the full $\delta^{18}O_P$ field as well as the subsets (Table 2). $\delta^{18}O_P$ EOF1 from the iLME $\delta^{18}O_P$ dynamic composites ($\delta^{18}O_P$ $\text{EOF1}_{\text{iLME-dyncomp}}$) is similar to global $\delta^{18}O_P$ EOF1 around the Pacific margin (points in Fig. 6c compared with points in Fig. 6d), with some differences in Europe and northern Africa where loadings are weaker. The strength of the correlation of the $\delta^{18}O_P$ $\text{PC1}_{\text{iLME-dyncomp}}$ with ΔSLP (0.62) is also similar to the strength of the correlation between global $\delta^{18}O_P$ PC1 and ΔSLP from observations (Table 2). The correlation of ΔSLP with the full-field, cluster centroid, and cluster mean $\delta^{18}O_P$ PC1s is stronger than with the dynamic composite $\delta^{18}O_P$ PC1. This suggests that the true imprint of the PWC in global $\delta^{18}O_P$ may be even stronger than seen in our composited station data.

The most obvious difference between the iCESM and observation-based analyses is in the ΔSLP index itself. In observations, ΔSLP is moderately strongly anti-correlated with the Niño 3.4 index (-0.78; Supp. Fig. 3), and global $\delta^{18}O_P$ PC1 is more strongly correlated with ΔSLP than the Niño 3.4 index (Table 1). In the iLME, ΔSLP is almost perfectly anti-correlated with the Niño 3.4 index (-0.98). This is consistent with previous work indicating an overly strong ENSO amplitude in CESM1 (Otto-Bliesner et al. 2016; Stevenson et al. 2016) and an overly active ENSO influence on other ocean basins in the iCESM (Midhun et al, 2020), although it also likely reflects noise inherent to observations-based data. Accordingly, the global $\delta^{18}O_P$ PC1 is slightly more strongly correlated with Niño 3.4 in iLME than in observations ($r = -0.6$ for the ‘dynamic composite’ subset, which is most comparable with the observation-based analysis).

4 Discussion

4.1 Relationship between global $\delta^{18}O_P$ patterns and the PWC

There is a clear imprint of the PWC in global $\delta^{18}O_P$ over the analysis interval (1982-2015) (Figs. 4 & 5, Table 1). This result is robust to our choice of PWC index, with similar results when using SLP gradients (ΔSLP and the SOI) or equatorial Pacific zonal wind anomalies as proxies for the strength of the PWC (Table 1). Even though global $\delta^{18}O_P$ PC1 did not *a priori* target the PWC, it reproduces the surface temperature, SLP, and precipitation anomalies associated with changes in the strength of the PWC (Fig. 5 compared with Fig. 3). Additionally, out of all possible isotope-climate mode relationships tested, global $\delta^{18}O_P$ PC1 is most strongly correlated with ΔSLP (Table 1). Although there is large variation in $\delta^{18}O_P$ anomaly patterns associated with single years of anomalously strong or weak PWC (Supp. Figs. 5, 6 & 7), the close relationship between global $\delta^{18}O_P$ PC1 and ΔSLP suggests a strong overall influence of the PWC on global circulation and associated spatio-temporal $\delta^{18}O_P$ patterns.

Notably, global $\delta^{18}O_P$ PC1 has a stronger relationship to atmospheric than oceanic variability in the equatorial Pacific (Table 1 top row compared with Table 1 middle row). This is not entirely surprising, given SST impacts must be transmitted to $\delta^{18}O_P$—both within the Pacific and in more remote teleconnected regions—via atmospheric processes including evaporation, moisture advection from the source, changes in atmospheric stability, and moisture transport aloft. The $\delta^{18}O$ of vapour in air parcels is further modified by atmospheric processes on multiple scales before final condensation and precipitation (Galewsky et al. 2016; Bowen et al. 2019). Changes in atmospheric circulation therefore have a more direct relationship with $\delta^{18}O_P$, even when they are driven in part by SST variability, for example in the case of ENSO.

Also of interest is that global precipitation PC1 has a weaker correlation with ΔSLP than global $\delta^{18}O_P$ PC1 (Table 1, correlation coefficients in parentheses). And unlike $\delta^{18}O_P$, the strength of correlations between global precipitation PC1 and the PWC are similar to correlations with the indices for tropical Pacific oceanic variability (i.e., ENSO). This suggests that whilst global annual-mean precipitation is influenced comparably by the SST and atmospheric circulation expressions of tropical Pacific climate variability, the isotopic composition of that precipitation responds more strongly to atmospheric circulation. In other words, whilst the PWC was already known to influence atmospheric circulation, our work demonstrates that $\delta^{18}O_P$ anomalies are more sensitive to this influence than precipitation anomalies.

4.2 Proposed mechanisms for the PWC imprint in global $\delta^{18}O_P$

The strong relationship between global $\delta^{18}O_P$ PC1 and ΔSLP probably arises through a combination of circulation features, including but not limited to ENSO and associated changes in the strength of atmospheric overturning circulation in the Pacific. These processes influence $\delta^{18}O_P$ around the Pacific and in teleconnected regions, via changes in precipitation amount, precipitation type, precipitation seasonality, storm organisation and intensity, and moisture source and transport path (Konecky et al. 2019; Galewsky et al. 2016; Bowen et al. 2019). For example, over the maritime continent and northern Australia, an increase in global $\delta^{18}O_P$ PC1 is associated with increased precipitation but decreased $\delta^{18}O_P$ (Fig. 5c). This is a region where ENSO-related large-scale atmospheric circulation changes produce a clear amount effect (Suwarman et al. 2017; Kurita et al. 2009; Conroy et al. 2013a). Additionally, a stronger PWC is associated with a southward shift of the southern margin of the Intertropical Convergence Zone over the maritime continent (Freitas et al. 2017), which increases precipitation over northern Australia and decreases $\delta^{18}O_P$ via an amount effect, and also increases the incidence of tropical cyclones, which typically have lower $\delta^{18}O_P$ than non-cyclonic rainfall (Hollins et al. 2018; Haig et al. 2014; Gedzelman et al. 2003; Lawrence and Gedzelman 1996). Likewise, the PWC influences the strength of the Australian monsoon, which in turn affects both tropical cyclone genesis and precipitation amounts in northern Australia (McBride and Keenan 1982). In short, $\delta^{18}O_P$ variability in this region reflects information about multiple large-scale atmospheric and oceanic processes with a strong connection to the PWC (Conroy et al. 2013b; Kurita et al. 2009).

The multiple complementary mechanisms by which the PWC can influence $\delta^{18}O_P$ are also evident in other regions. For example, in south-eastern China and south-east Asia, interannual variability in $\delta^{18}O_P$ is negatively correlated with the PWC, via dynamical mechanisms including changes in convection intensity (Cai and Tian 2016b; Ruan et al. 2019; Cai et al. 2017), changes in moisture source region and transport distance (Sun et al. 2018; Tan 2014; Ishizaki et al. 2012; Wolf et al. 2020), and via an amount effect (Ichiyanagi and Yamanaka 2005). While these are only two regional examples, there are clearly many mechanisms by which PWC strength could contribute to a single local loading pattern in our global $\delta^{18}O_P$ EOF1.

Theoretical and site-level studies outline many possible mechanisms for the observed PWC imprint in extratropical $\delta^{18}O_P$—including locations without a strong amount effect. For instance, over North America, precipitation and wind anomalies associated with an increase in global

$\delta^{18}O_P$ PC1 suggest a northward shift of the climatological westerlies (Fig. 5). This is similar to the relationship of the westerlies with ENSO, where during La Niña events, a high pressure anomaly develops over the north Pacific, steering the storm track northward and leading to reduced precipitation across southern North America (Ellis and Barton 2012; Johnson et al. 2020; Liu and Alexander 2007), and also resulting in a larger proportion of precipitation over central North America sourced from the Pacific Ocean (Berkelhammer et al. 2012). $\delta^{18}O_P$ in south-western North America depends in part on the moisture source region, where precipitation coming from easterly or proximal south-westerly sources generally has higher $\delta^{18}O_P$, whilst precipitation from westerly sources (the north Pacific) generally has lower $\delta^{18}O_P$ (Hu and Dominguez 2015; Liu et al. 2014; Friedman et al. 1992; Berkelhammer et al. 2012; McCabe-Glynn et al. 2013). These mechanisms likely all contribute to the North American $\delta^{18}O_P$ loading pattern. The PWC imprint in $\delta^{18}O_P$ in western Europe, north-western Africa, and southern South America is relatively weak (e.g. weaker loadings of these sites on global $\delta^{18}O_P$ PC1 in Fig. 4a). Temperature and/or precipitation anomalies in these regions have been linked to the tropical Pacific via teleconnections (e.g. Rimbu et al. 2003; Nicholson and Selato 2000; Nicholson and Kim 1997; Chiang and Sobel 2002; Lin and Qian 2019; Oehrlein et al. 2019; Shaman 2014; Brönnimann et al. 2006; Rutllant and Fuenzalida 2007; Tedeschi et al. 2013; Aceituno 1988; Strub et al. 2019), although relationships between the PWC and climate in these remote regions are likely non-linear (Wu and Hsieh 2004; Domeisen et al. 2019) and non-stationary (Rimbu et al. 2003).

4.3 $\delta^{18}O_P$ and the PWC in iCESM

PC1 of the subsampled iLME $\delta^{18}O_P$ is similar to PC1 of the fully sampled $\delta^{18}O_P$ field (Fig. 6, Table 2), particularly in the case of the spatially (but not temporally) subsampled data. This gives confidence that our results are not biased by the location of the observations, but rather faithfully represent global $\delta^{18}O_P$ variability. The $\delta^{18}O_P$ response to changes in ΔSLP in the iLME is also consistent with observations (Table 2), as are the precipitation and SLP anomalies associated with global $\delta^{18}O_P$ PC1 within the iLME (Fig. 7). The similarity of the $\delta^{18}O_P$-ΔSLP relationship in the model and observations suggests that the response of $\delta^{18}O_P$ to changes in the strength of the PWC is well simulated by iCESM. The $\delta^{18}O_P$ spatial fingerprinting analysis also demonstrates that iCESM accurately captures the diversity of $\delta^{18}O_P$ anomaly patterns associated with the most positive and negative ΔSLP anomalies (Supp. Fig. 7 compared with Supp. Figs 5 and 6). iCESM simulations are therefore a useful tool with which to delve deeper into the dynamical processes linking the PWC and the global water cycle, and this will be leveraged in future work.

4.4 Relationship of global $\delta^{18}O_P$ variability with GMST

Palaeoclimate proxy data suggest that on *millennial* time scales, $\delta^{18}O$ of the global meteoric water pool primarily reflects the thermodynamic component of the global water cycle, where global $\delta^{18}O$ increases along with GMST (Falster et al. 2019). However, GMST and global $\delta^{18}O_P$ PC1 are not significantly correlated over the interval that we examined (Supp. Fig. 9). Considering this lack of obvious GMST influence, combined with the strong imprint of the PWC in global $\delta^{18}O_P$, our results suggest that on interannual to decadal time scales, global $\delta^{18}O_P$ patterns record more information about regional- to large-scale atmosphere-ocean dynamics than the global thermodynamic component of the water cycle.

5 Conclusions

On interannual to decadal timescales, the PWC has a dominant impact on global spatio-temporal patterns of $\delta^{18}O_P$ variability. Given that $\delta^{18}O_P$ integrates information from all parts of the water cycle, we conclude that the regional expressions of global water cycle variability are linked to changes in tropical Pacific atmospheric circulation. Hence, whilst previous studies demonstrated that the globally-averaged water cycle will intensify with future warming, our results suggest that uncertainty in future changes in PWC trend and variability (Plesca et al. 2018) may translate to uncertainty in the regional-scale hydroclimate response to global warming, even in areas where PWC teleconnections to precipitation amount are not as readily apparent.

Regional-scale hydroclimate variability associated with changes in the strength of the PWC manifests as changes in moisture source and transport path, seasonality, precipitation type, degree of storm organisation, and other dynamical processes, rather than simply changes in local precipitation amount. Our findings therefore highlight the usefulness of $\delta^{18}O_P$ (and by extension, also $\delta^{2}H_P$) as a single variable able to characterise changes in the fundamental processes underlying hydroclimate variability, at a global scale. The sensitivity of $\delta^{18}O_P$ to many different processes means that isotope-enabled climate models will continue to offer more detailed insights into the global water cycle and its response to climate change (Dee et al. 2018; Nusbaumer et al. 2017; Nusbaumer and Noone 2018). Additionally, the clear imprint of the

PWC in global $\delta^{18}O_P$ provides new avenues for exploring PWC variability, both in the recent past and on longer timescales, via water isotope proxy data.

Data availability statement

All data used in this study are freely available from online repositories. $\delta^{18}O_P$ data were downloaded from:

- GNIP: https://nucleus.iaea.org/wiser
- wiDB: https://waterisotopesDB.org
- ANSTO: https://research-data.ansto.gov.au/collection/881

Gridded observational and reanalysis datasets used in this study are available at:

- GPCC: https://psl.noaa.gov/data/gridded/data.gpcc.html
- CPC CMAP: https://psl.noaa.gov/data/gridded/data.cmap.html
- Berkeley Earth surface temperature: http://berkeleyearth.org/data/
- HadSLP2 and ERSSTv5: https://psl.noaa.gov/
- WASWind: https://rda.ucar.edu/datasets/ds232.3/
- ERA5: https://cds.climate.copernicus.eu/cdsapp#!/dataset/reanalysis-era5-pressure-levels-monthly-means?tab=overview

Climate indices used in this study (other than those calculated by the authors) are available at:

- SOI: http://www.bom.gov.au/climate/enso/soi/
- DMI: https://psl.noaa.gov/gcos_wgsp/Timeseries/DMI/
- SAM: https://www.cpc.ncep.noaa.gov/products/precip/CWlink/daily_ao_index/aao/aao.shtml
- GMST: https://data.giss.nasa.gov/gistemp/

Acknowledgements

This research was supported by a National Science Foundation (NSF) P2C2 grants AGS-1805141 to Washington University in St. Louis, AGS-1805143 to the University of California, Santa Barbara, and AGS-2041281 to the University of Hawai'i. The CESM project is supported primarily by the NSF. Computing and data storage resources used for iCESM analyses, including the Cheyenne supercomputer (doi:10.5065/D6RX99HX), were provided by the Computational and Information Systems Laboratory (CISL) at NCAR. Thanks to Nick McKay for sharing the R code that we used for the dynamic compositing. Thanks also to three anonymous reviewers, whose insightful comments lead to improvements in this paper.

References

Aceituno, P., 1988: On the Functioning of the Southern Oscillation in the South American Sector. Part I: Surface Climate. *Mon. Weather Rev.*, **116**, 505–524.

Aggarwal, P. K., U. Romatschke, and L. Araguas-Araguas, 2016: Proportions of convective and stratiform precipitation revealed in water isotope ratios. *Nature*,.

Alexander, M. A., I. Bladé, M. Newman, J. R. Lanzante, N.-C. Lau, and J. D. Scott, 2002: The Atmospheric Bridge: The Influence of ENSO Teleconnections on Air–Sea Interaction over the Global Oceans. *J. Clim.*, **15**, 2205–2231.

Allan, R., and T. Ansell, 2006: A New Globally Complete Monthly Historical Gridded Mean Sea Level Pressure Dataset (HadSLP2): 1850–2004. *J. Clim.*, **19**, 5816–5842.

Allan, R. P., and Coauthors, 2020: Advances in understanding large-scale responses of the water cycle to climate change. *Annals of the New York Academy of Sciences*, **1472**, 49–75, https://doi.org/10.1111/nyas.14337.

Allen, M. R., and W. J. Ingram, 2002: Constraints on future changes in climate and the hydrologic cycle. *Nature*, **419**, 224–232.

Araguás-Araguás, L., K. Froehlich, and K. Rozanski, 2000: Deuterium and oxygen-18 isotope composition of precipitation and atmospheric moisture. *Hydrol. Process.*, **14**, 1341–1355.

Ashok, K., S. K. Behera, S. A. Rao, H. Weng, and T. Yamagata, 2007: El Niño Modoki and its possible teleconnection. *J. Geophys. Res.*, **112**, 505.

Batehup, R., S. McGregor, and A. J. E. Gallant, 2015: The influence of non-stationary teleconnections on palaeoclimate reconstructions of ENSO variance using a pseudoproxy framework. *Clim. Past*, **11**.

Becker, A., P. Finger, A. Meyer-Christoffer, B. Rudolf, K. Schamm, U. Schneider, and M. Ziese, 2013: A description of the global land-surface precipitation data products of the Global Precipitation Climatology Centre with sample applications including centennial (trend) analysis from 1901–present. *Earth System Science Data*, **5**, 71–99, https://doi.org/10.5194/essd-5-71-2013.

Beckers, J.-M., A. Barth, and A. Alvera-Azcárate, 2006: DINEOF reconstruction of clouded images including error maps? application to the Sea-Surface Temperature around Corsican Island.

Benjamini, Y., and Y. Hochberg, 1995: Controlling the false discovery rate: A practical and powerful approach to multiple testing. *J. R. Stat. Soc.*, **57**, 289–300.

Berkelhammer, M., L. Stott, K. Yoshimura, K. Johnson, and A. Sinha, 2012: Synoptic and mesoscale controls on the isotopic composition of precipitation in the western United States. *Clim. Dyn.*, **38**, 433–454.

Bjerknes, J., 1969: Atmospheric teleconnections from the equatorial Pacific. *Mon. Weather Rev.*, **97**, 163–172.

Bowen, G. J., 2008: Spatial analysis of the intra-annual variation of precipitation isotope ratios and its climatological corollaries. *J. Geophys. Res. D: Atmos.*, **113**.

——, and B. Wilkinson, 2002: Spatial distribution of δ18O in meteoric precipitation. *Geology*, **30**, 315–318.

——, Z. Cai, R. P. Fiorella, and A. L. Putman, 2019: Isotopes in the Water Cycle: Regional- to Global-Scale Patterns and Applications. *Annu. Rev. Earth Planet. Sci.*, https://doi.org/10.1146/annurev-earth-053018-060220.

Brady, E., and Coauthors, 2019: The Connected Isotopic Water Cycle in the Community Earth System Model Version 1. *Journal of Advances in Modeling Earth Systems*, **11**, 2547–2566.

Braganza, K., J. L. Gergis, S. B. Power, J. S. Risbey, and A. M. Fowler, 2009: A multiproxy index of the El Niño--Southern Oscillation, AD 1525--1982. *J. Geophys. Res. D: Atmos.*, **114**.

Brönnimann, S., E. Xoplaki, C. Casty, A. Pauling, and J. Luterbacher, 2006: ENSO influence on Europe during the last centuries. *Climate Dynamics*, **28**, 181–197, https://doi.org/10.1007/s00382-006-0175-z.

Brown, J., I. Simmonds, and D. Noone, 2006: Modeling δ18O in tropical precipitation and the surface ocean for present-day climate. *J. Geophys. Res. D: Atmos.*, **111**.

Cai, Z., and L. Tian, 2016a: Processes Governing Water Vapor Isotope Composition in the Indo-Pacific Region: Convection and Water Vapor Transport. *J. Clim.*, **29**, 8535–8546.

——, and ——, 2016b: Atmospheric Controls on Seasonal and Interannual Variations in the Precipitation Isotope in the East Asian Monsoon Region. *J. Clim.*, **29**, 1339–1352.

Cai, Z., L. Tian, and G. J. Bowen, 2017: ENSO variability reflected in precipitation oxygen isotopes across the Asian Summer Monsoon region. *Earth Planet. Sci. Lett.*,.

Capotondi, A., and Coauthors, 2015: Understanding ENSO Diversity. *Bull. Am. Meteorol. Soc.*, **96**, 921–938.

Cheng, L., and Coauthors, 2020: Improved Estimates of Changes in Upper Ocean Salinity and the Hydrological Cycle. *J. Clim.*, **33**, 10357–10381.

Chiang, J. C. H., and A. H. Sobel, 2002: Tropical Tropospheric Temperature Variations Caused by ENSO and Their Influence on the Remote Tropical Climate*. *Journal of Climate*, **15**, 2616–2631, https://doi.org/10.1175/1520-0442(2002)015<2616:tttvcb>2.0.co;2.

Chiang, J. C. H., and D. J. Vimont, 2004: Analogous meridional modes of atmosphere--ocean variability in the tropical Pacific and tropical Atlantic. *J. Clim.*, **17**, 4143–4158.

Chou, C., and C.-W. Lan, 2012: Changes in the Annual Range of Precipitation under Global Warming. *J. Clim.*, **25**, 222–235.

Chung, E.-S., A. Timmermann, B. J. Soden, K.-J. Ha, L. Shi, and V. O. John, 2019: Reconciling opposing Walker circulation trends in observations and model projections. *Nature Climate Change*, **9**, 405–412, https://doi.org/10.1038/s41558-019-0446-4.

Clarke, A. J., and A. Lebedev, 1996: Long-Term Changes in the Equatorial Pacific Trade Winds. *J. Clim.*, **9**, 1020–1029.

Coats, S., J. E. Smerdon, B. I. Cook, and R. Seager, 2013: Stationarity of the tropical pacific teleconnection to North America in CMIP5/PMIP3 model simulations. *Geophys. Res. Lett.*, **40**, 4927–4932.

Cole, J. E., and E. R. Cook, 1998: The changing relationship between ENSO variability and moisture balance in the continental United States. *Geophys. Res. Lett.*, **25**, 4529–4532.

Conroy, J. L., K. M. Cobb, and D. Noone, 2013a: Comparison of precipitation isotope variability across the tropical Pacific in observations and SWING2 model simulations. *J. Geophys. Res.*,.

Conroy, J. L., K. M. Cobb, and D. Noone, 2013b: Comparison of precipitation isotope variability across the tropical Pacific in observations and SWING2 model simulations. *J. Geophys. Res. D: Atmos.*, **118**, 5867–5892.

——, D. Noone, K. M. Cobb, J. W. Moerman, and B. L. Konecky, 2016: Paired stable isotopologues in precipitation and vapor: A case study of the amount effect within western tropical Pacific storms. *J. Geophys. Res. D: Atmos.*, **121**, 3290–3303.

Copernicus Climate Change Service (C3S), 2017: ERA5: Fifth generation of ECMWF atmospheric reanalyses of the global climate. https://cds.climate.copernicus.eu/cdsapp#!/home (Accessed August 2020).

Dagan, G., P. Stier, and D. Watson-Parris, 2019: Analysis of the Atmospheric Water Budget for Elucidating the Spatial Scale of Precipitation Changes Under Climate Change. *Geophys. Res. Lett.*, **46**, 10504–10511.

Dai, A., K. E. Trenberth, and T. R. Karl, 1998: Global variations in droughts and wet spells: 1900-1995. *Geophys. Res. Lett.*, **25**, 3367–3370.

——, T. Qian, K. E. Trenberth, and J. D. Milliman, 2009: Changes in Continental Freshwater Discharge from 1948 to 2004. *J. Clim.*, **22**, 2773–2792.

——, J. Wang, P. W. Thorne, D. E. Parker, L. Haimberger, and X. L. Wang, 2011: A New Approach to Homogenize Daily Radiosonde Humidity Data. *J. Clim.*, **24**, 965–991.

——, J. C. Fyfe, S.-P. Xie, and X. Dai, 2015: Decadal modulation of global surface temperature by internal climate variability. *Nature Climate Change*, **5**, 555–559, https://doi.org/10.1038/nclimate2605.

Dansgaard, W., 1964: Stable isotopes in precipitation. *Tellus*, **16**, 436–468, https://doi.org/10.1111/j.2153-3490.1964.tb00181.x.

Dee, S. G., J. Nusbaumer, A. Bailey, J. M. Russell, J.-E. Lee, B. Konecky, N. H. Buenning, and D. C. Noone, 2018: Tracking the Strength of the Walker Circulation with Stable Isotopes in Water Vapor. *J. Geophys. Res. D: Atmos.*, **123**, 7254–7270.

Del Genio, A. D., A. A. Lacis, and R. A. Ruedy, 1991: Simulations of the effect of a warmer climate on atmospheric humidity. *Nature*, **351**, 382–385.

Deser, C., and J. M. Wallace, 1990: Large-Scale Atmospheric Circulation Features of Warm and Cold Episodes in the Tropical Pacific. *J. Clim.*, **3**, 1254–1281.

DiNezio, P., A. Clement, and G. Vecchi, 2010: Reconciling differing views of tropical pacific climate change. *Eos*, **91**, 141–142.

DiNezio, P. N., G. A. Vecchi, and A. C. Clement, 2013: Detectability of Changes in the Walker Circulation in Response to Global Warming. *J. Clim.*, **26**, 4038–4048.

Domeisen, D. I. V., C. I. Garfinkel, and A. H. Butler, 2019: The Teleconnection of El Niño Southern Oscillation to the Stratosphere. *Reviews of Geophysics*, **57**, 5–47, https://doi.org/10.1029/2018rg000596.

Dong, L., and M. J. McPhaden, 2017: The role of external forcing and internal variability in regulating global mean surface temperatures on decadal timescales. *Environ. Res. Lett.*, **12**, 034011.

Durack, P. J., S. E. Wijffels, and R. J. Matear, 2012: Ocean salinities reveal strong global water cycle intensification during 1950 to 2000. *Science*, **336**, 455–458.

Ellis, A. W., and N. P. Barton, 2012: Characterizing the North Pacific Jet Stream for Understanding Historical Variability in Western United States Winter Precipitation. *Physical Geography*, **33**, 105–128.

England, M. H., and Coauthors, 2014: Recent intensification of wind-driven circulation in the Pacific and the ongoing warming hiatus. *Nat. Clim. Chang.*, **4**, 222–227.

Falster, G., and Coauthors, 2019: New insights into spatial and temporal dynamics of the global water cycle from the Iso2k database. Vol. 2019 of, PP41A – 04.

Freitas, A. C. V., L. Aímola, T. Ambrizzi, and C. P. de Oliveira, 2017: Extreme Intertropical Convergence Zone shifts over Southern Maritime Continent. *Atmos. Sci. Lett.*, **18**, 2–10.

Friedman, I., G. I. Smith, J. D. Gleason, A. Warden, and J. M. Harris, 1992: Stable isotope composition of waters in southeastern California 1. Modern precipitation. *Journal of Geophysical Research*, **97**, 5795, https://doi.org/10.1029/92jd00184.

Galewsky, J., H. C. Steen-Larsen, and R. D. Field, 2016: Stable isotopes in atmospheric water vapor and applications to the hydrologic cycle. *Reviews of*,.

Gedzelman, S., and Coauthors, 2003: Probing Hurricanes with Stable Isotopes of Rain and Water Vapor. *Mon. Weather Rev.*, **131**, 1112–1127.

GISTEMP Team, 2020: GISS Surface Temperature Analysis (GISTEMP), version 4. https://data.giss.nasa.gov/gistemp/ (Accessed December 1, 2020).

Graf, P., H. Wernli, S. Pfahl, and H. Sodemann, 2019: A new interpretative framework for below-cloud effects on stable water isotopes in vapour and rain.

Greve, P., B. Orlowsky, B. Mueller, J. Sheffield, M. Reichstein, and S. I. Seneviratne, 2014: Global assessment of trends in wetting and drying over land. *Nat. Geosci.*, **7**, 716–721.

Haig, J., J. Nott, and G.-J. Reichart, 2014: Australian tropical cyclone activity lower than at any time over the past 550-1,500 years. *Nature*, **505**, 667–671.

Han, Z., Q. Zhang, Q. Wen, Z. Lu, G. Feng, T. Su, Q. Li, and Q. Zhang, 2020: The changes in ENSO-induced tropical Pacific precipitation variability in the past warm and cold climates from the EC-Earth simulations. *Clim. Dyn.*,.

Hegerl, G. C., and Coauthors, 2015: Challenges in Quantifying Changes in the Global Water Cycle. *Bull. Am. Meteorol. Soc.*, **96**, 1097–1115.

Held, I. M., and B. J. Soden, 2006: Robust Responses of the Hydrological Cycle to Global Warming. *J. Clim.*, **19**, 5686–5699.

Hollins, S. E., C. E. Hughes, J. Crawford, D. I. Cendón, and K. T. Meredith, 2018: Rainfall isotope variations over the Australian continent--implications for hydrology and isoscape applications. *Sci. Total Environ.*, **645**, 630–645.

Hou, X., J. Cheng, S. Hu, and G. Feng, 2018: Interdecadal Variations in the Walker Circulation and Its Connection to Inhomogeneous Air Temperature Changes from 1961–2012. *Atmosphere*, **9**, 469, https://doi.org/10.3390/atmos9120469.

Huang, B., and Coauthors, 2017: NOAA Extended Reconstructed Sea Surface Temperature (ERSST), Version 5. https://doi.org/10.7289/V5T72FNM.

Hu, H., and F. Dominguez, 2015: Evaluation of Oceanic and Terrestrial Sources of Moisture for the North American Monsoon Using Numerical Models and Precipitation Stable Isotopes. *J. Hydrometeorol.*, **16**, 19–35.

Huntington, T. G., 2006: Evidence for intensification of the global water cycle: Review and synthesis. *J. Hydrol.*, **319**, 83–95.

IAEA/WMO, 2020: Global Network of Isotopes in Precipitation. The GNIP Database. https://nucleus.iaea.org/wiser.

Ichiyanagi, K., and M. D. Yamanaka, 2005: Interannual variation of stable isotopes in precipitation at Bangkok in response to El Niño Southern Oscillation. *Hydrological Processes: An*,.

Ishizaki, Y., K. Yoshimura, and S. Kanae, 2012: Interannual variability of H218O in precipitation over the Asian monsoon region. *Journal of*,.

Johnson, Z. F., Y. Chikamoto, S.-Y. S. Wang, M. J. McPhaden, and T. Mochizuki, 2020: Pacific decadal oscillation remotely forced by the equatorial Pacific and the Atlantic Oceans. *Clim. Dyn.*, **55**, 789–811.

Kang, S. M., S.-P. Xie, Y. Shin, H. Kim, Y.-T. Hwang, M. F. Stuecker, B. Xiang, and M. Hawcroft, 2020: Walker circulation response to extratropical radiative forcing. *Sci Adv*, **6**, https://doi.org/10.1126/sciadv.abd3021.

Kaufman, D., N. McKay, C. Routson, M. Erb, C. Dätwyler, P. S. Sommer, O. Heiri, and B. Davis, 2020: Holocene global mean surface temperature, a multi-method reconstruction approach. *Sci Data*, **7**, 201.

Konecky, B. L., D. C. Noone, and K. M. Cobb, 2019: The Influence of Competing Hydroclimate Processes on Stable Isotope Ratios in Tropical Rainfall. *Geophys. Res. Lett.*, **46**, 1622–1633.

Kong, W., and J. C. H. Chiang, 2020: Southward Shift of Westerlies Intensifies the East Asian Early Summer Rainband Following El Niño. *Geophys. Res. Lett.*, **47**, 201715386.

Kosaka, Y., and S.-P. Xie, 2013: Recent global-warming hiatus tied to equatorial Pacific surface cooling. *Nature*, **501**, 403–407.

Kurita, N., 2013: Water isotopic variability in response to mesoscale convective system over the tropical ocean. *J. Geophys. Res. D: Atmos.*, **118**, 10–376.

——, K. Ichiyanagi, J. Matsumoto, M. D. Yamanaka, and T. Ohata, 2009: The relationship between the isotopic content of precipitation and the precipitation amount in tropical regions. *Journal of Geochemical Exploration*, **102**, 113–122, https://doi.org/10.1016/j.gexplo.2009.03.002.

Lawrence, R. J., and D. S. Gedzelman, 1996: Low stable isotope ratios of tropical cyclone rains. *Geophys. Res. Lett.*, **23**, 527–530.

Lenssen, N. J. L., G. A. Schmidt, J. E. Hansen, M. J. Menne, A. Persin, R. Ruedy, and D. Zyss, 2019: Improvements in the GISTEMP Uncertainty Model. *J. Geophys. Res. D: Atmos.*, **124**, 6307–6326.

Lin, J., and T. Qian, 2019: A New Picture of the Global Impacts of El Nino-Southern Oscillation. *Sci. Rep.*, **9**, 17543.

Liu, Z., and M. Alexander, 2007: Atmospheric bridge, oceanic tunnel, and global climatic teleconnections. *Rev. Geophys.*, **45**, 1769.

Liu, Z., K. Yoshmura, G. J. Bowen, and J. M. Welker, 2014: Pacific–North American Teleconnection Controls on Precipitation Isotopes (δ18O) across the Contiguous United States and Adjacent Regions: A GCM-Based Analysis. *J. Clim.*, **27**, 1046–1061.

McBride, J. L., and T. D. Keenan, 1982: Climatology of tropical cyclone genesis in the Australian region. *J. Climatol.*, **2**, 13–33.

McCabe-Glynn, S., K. R. Johnson, C. Strong, M. Berkelhammer, A. Sinha, H. Cheng, and R. L. Edwards, 2013: Variable North Pacific influence on drought in southwestern North America since AD 854. *Nat. Geosci.*, **6**, 617–621.

Meehl, G. A., F. Zwiers, J. Evans, T. Knutson, L. Mearns, and P. Whetton, 2000: Trends in Extreme Weather and Climate Events: Issues Related to Modeling Extremes in Projections of Future Climate Change. *Bull. Am. Meteorol. Soc.*, **81**, 427–436.

Misios, S., L. J. Gray, M. F. Knudsen, C. Karoff, H. Schmidt, and J. D. Haigh, 2019: Slowdown of the Walker circulation at solar cycle maximum. *Proc. Natl. Acad. Sci. U. S. A.*, **116**, 7186–7191.

Moore, M., Z. Kuang, and P. N. Blossey, 2014: A moisture budget perspective of the amount effect. *Geophysical Research Letters*, **41**, 1329–1335, https://doi.org/10.1002/2013gl058302.

Nicholson, S., and J. C. Selato, 2000: The influence of La Niña on African Rainfall. *Int. J. Climatol.*, **20**, 1761–1776.

Nicholson, S. E., and J. Kim, 1997: The Relationship of the El Niño-Southern Oscillation to African Rainfall. *International Journal of Climatology*, **17**, 117–135.

Norris, J., G. Chen, and J. D. Neelin, 2019: Thermodynamic versus Dynamic Controls on Extreme Precipitation in a Warming Climate from the Community Earth System Model Large Ensemble. *J. Clim.*, **32**, 1025–1045.

Nusbaumer, J., and D. Noone, 2018: Numerical Evaluation of the Modern and Future Origins of Atmospheric River Moisture over the West Coast of the United States. *J. Geophys. Res. D: Atmos.*, **123**, 6423–6442.

——, T. E. Wong, C. Bardeen, and D. Noone, 2017: Evaluating hydrological processes in the C ommunity A tmosphere M odel V ersion 5 (C AM5) using stable isotope ratios of water. *Journal of Advances in Modeling Earth Systems*, **9**, 949–977.

Oehrlein, J., G. Chiodo, and L. M. Polvani, 2019: Separating and quantifying the distinct impacts of El Niño and sudden stratospheric warmings on North Atlantic and Eurasian wintertime climate. *Atmospheric Science Letters*, **20**, e923, https://doi.org/10.1002/asl.923.

O'Gorman, P. A., 2015: Precipitation Extremes Under Climate Change. *Current Climate Change Reports*, **1**, 49–59, https://doi.org/10.1007/s40641-015-0009-3.

Otto-Bliesner, B. L., and Coauthors, 2016: Climate Variability and Change since 850 CE: An Ensemble Approach with the Community Earth System Model. *Bull. Am. Meteorol. Soc.*, **97**, 735–754.

Pfahl, S., P. A. O'Gorman, and E. M. Fischer, 2017: Understanding the regional pattern of projected future changes in extreme precipitation. *Nat. Clim. Chang.*, **7**, 423–427.

Plesca, E., V. Grützun, and S. A. Buehler, 2018: How Robust Is the Weakening of the Pacific Walker Circulation in CMIP5 Idealized Transient Climate Simulations? *J. Clim.*, **31**, 81–97.

Putman, A. L., and G. J. Bowen, 2019: A global database of the stable isotopic ratios of meteoric and terrestrial waters. *Hydrol. Earth Syst. Sci.*, **23**, 4389–4396.

Putman, A. L., R. P. Fiorella, and G. J. Bowen, 2019: A global perspective on local meteoric water lines: Meta-analytic insight into fundamental controls and practical constraints. *Water Resour.*,.

Putman, A. L., G. J. Bowen, and C. Strong, 2021: Local and regional modes of hydroclimatic change expressed in modern multidecadal precipitation oxygen isotope trends. *Geophys. Res. Lett.*, https://doi.org/10.1029/2020gl092006.

Rimbu, N., G. Lohmann, T. Felis, and J. Pätzold, 2003: Shift in ENSO Teleconnections Recorded by a Northern Red Sea Coral. *Journal of Climate*, **16**, 1414–1422, https://doi.org/10.1175/1520-0442-16.9.1414.

Risi, C., S. Bony, and F. Vimeux, 2010: Water-stable isotopes in the LMDZ4 general circulation model: Model evaluation for present-day and past climates and applications to climatic interpretations of …. *J. Geophys. Res.*,.

Rohde, R. A., and Z. Hausfather, 2020: The Berkeley Earth Land/Ocean Temperature Record. *Earth System Science Data*, **12**, 3469–3479, https://doi.org/10.5194/essd-12-3469-2020.

Ropelewski, C. F., and M. S. Halpert, 1987: Global and Regional Scale Precipitation Patterns Associated with the El Niño/Southern Oscillation. *Mon. Weather Rev.*, **115**, 1606–1626.

——, and ——, 1989: Precipitation Patterns Associated with the High Index Phase of the Southern Oscillation. *J. Clim.*, **2**, 268–284.

Ropelewski, C. F., and M. S. Halpert, 1996: Quantifying Southern Oscillation-Precipitation Relationships. *J. Clim.*, **9**, 1043–1059.

Rozanski, K., L. Araguás-Araguás, and R. Gonfiantini, 1993: Isotopic patterns in modern global precipitation. *Washington DC American Geophysical Union Geophysical Monograph Series*, **78**, 1.

Ruan, J., H. Zhang, Z. Cai, X. Yang, and J. Yin, 2019: Regional controls on daily to interannual variations of precipitation isotope ratios in Southeast China: Implications for paleomonsoon reconstruction. *Earth Planet. Sci. Lett.*,.

Rutllant, J., and H. Fuenzalida, 2007: Synoptic aspects of the central chile rainfall variability associated with the southern oscillation. *International Journal of Climatology*, **11**, 63–76, https://doi.org/10.1002/joc.3370110105.

Samuels-Crow, K. E., J. Galewsky, D. R. Hardy, Z. D. Sharp, J. Worden, and C. Braun, 2014: Upwind convective influences on the isotopic composition of atmospheric water vapor over the tropical Andes. *J. Geophys. Res. D: Atmos.*, **119**, 7051–7063.

Schlosser, C. A., and P. R. Houser, 2007: Assessing a Satellite-Era Perspective of the Global Water Cycle. *J. Clim.*, **20**, 1316–1338.

Schneider, U., P. Finger, A. Meyer-Christoffer, E. Rustemeier, M. Ziese, and A. Becker, 2017: Evaluating the Hydrological Cycle over Land Using the Newly-Corrected Precipitation Climatology from the Global Precipitation Climatology Centre (GPCC). *Atmosphere* , **8**, 52.

Seager, R., N. Naik, and G. A. Vecchi, 2010: Thermodynamic and Dynamic Mechanisms for Large-Scale Changes in the Hydrological Cycle in Response to Global Warming. *J. Clim.*, **23**, 4651–4668.

Shaman, J., 2014: The Seasonal Effects of ENSO on European Precipitation: Observational Analysis. *Journal of Climate*, **27**, 6423–6438, https://doi.org/10.1175/jcli-d-14-00008.1.

Skliris, N., J. D. Zika, G. Nurser, S. A. Josey, and R. Marsh, 2016: Global water cycle amplifying at less than the Clausius-Clapeyron rate. *Scientific Reports*, **6**, https://doi.org/10.1038/srep38752.

Soden, B. J., 2000: The Sensitivity of the Tropical Hydrological Cycle to ENSO. *J. Clim.*, **13**, 538–549.

Stephens, G. L., and Y. Hu, 2010: Are climate-related changes to the character of global-mean precipitation predictable? *Environ. Res. Lett.*, **5**, 025209.

Stevenson, S., A. Timmermann, Y. Chikamoto, S. Langford, and P. DiNezio, 2015: Stochastically Generated North American Megadroughts. *J. Clim.*, **28**, 1865–1880.

——, B. Otto-Bliesner, J. Fasullo, and E. Brady, 2016: “El Niño Like” Hydroclimate Responses to Last Millennium Volcanic Eruptions. *J. Clim.*, **29**, 2907–2921.

Stevenson, S., B. L. Otto-Bliesner, E. C. Brady, J. Nusbaumer, C. Tabor, R. Tomas, D. C. Noone, and Z. Liu, 2019: Volcanic Eruption Signatures in the Isotope-Enabled Last Millennium Ensemble. *Paleoceanography and Paleoclimatology*, **34**, 1534–1552.

Stewart, M. K., 1975: Stable isotope fractionation due to evaporation and isotopic exchange of falling waterdrops: Applications to atmospheric processes and evaporation of lakes. *Journal of Geophysical Research*, **80**, 1133–1146, https://doi.org/10.1029/jc080i009p01133.

Strub, P. T., P. Ted Strub, C. James, V. Montecino, J. A. Rutllant, and J. L. Blanco, 2019: Ocean circulation along the southern Chile transition region (38°–46°S): Mean, seasonal and interannual variability, with a focus on 2014–2016. *Progress in Oceanography*, **172**, 159–198, https://doi.org/10.1016/j.pocean.2019.01.004.

Sun, Z., Y. Yang, J. Zhao, N. Tian, and X. Feng, 2018: Potential ENSO effects on the oxygen isotope composition of modern speleothems: Observations from Jiguan Cave, central China. *J. Hydrol.*,.

Sutanto, S. J., G. Hoffmann, J. Worden, R. A. Scheepmaker, I. Aben, and T. Roeckmann, 2015: Atmospheric processes governing the changes in water isotopologues during ENSO events from model and satellite measurements. *J. Geophys. Res. D: Atmos.*, **120**, 6712–6729.

Suwarman, R., K. Ichiyanagi, T. Masahiro, K. Yoshimura, S. Mori, M. D. Yamanaka, F. Syamsudin, and H. A. Belgaman, 2017: El Niño Southern Oscillation Signature in Atmospheric Water Isotopes over Maritime Continent during Wet Season. *Journal of the Meteorological Society of Japan*, **advpub**, https://doi.org/10.2151/jmsj.2017-003.

Tan, M., 2014: Circulation effect: response of precipitation δ 18 O to the ENSO cycle in monsoon regions of China. *Clim. Dyn.*, **42**, 1067–1077.

Tedeschi, R. G., I. F. A. Cavalcanti, and A. M. Grimm, 2013: Influences of two types of ENSO on South American precipitation. *International Journal of Climatology*, **33**, 1382–1400, https://doi.org/10.1002/joc.3519.

Terzer, S., L. I. Wassenaar, L. J. Araguás-Araguás, P. K. Aggarwal, and Others, 2013: Global isoscapes for δ18O and δ2H in precipitation: improved prediction using regionalized climatic regression models. *Hydrol. Earth Syst. Sci.*, **17**, 4713–4728.

Tian, Z., and D. Jiang, 2020: Weakening and eastward shift of the tropical Pacific Walker circulation during the Last Glacial Maximum. *Boreas*, **49**, 200–210.

Tokinaga, H., 2012: Wave and Anemometer-based Sea Surface Wind (WASWind). https://doi.org/10.5065/BRX8-V029.

Trenberth, K. E., L. Smith, T. Qian, A. Dai, and J. Fasullo, 2007: Estimates of the Global Water Budget and Its Annual Cycle Using Observational and Model Data. *J. Hydrometeorol.*, **8**, 758–769.

Troup, A. J., 1965: The “southern oscillation.” *Quart. J. Roy. Meteor. Soc.*,.

Vecchi, G. A., and B. J. Soden, 2007: Global warming and the weakening of the tropical circulation. *J. Clim.*, **20**, 4316–4340.

——, ——, A. T. Wittenberg, I. M. Held, A. Leetmaa, and M. J. Harrison, 2006: Weakening of tropical Pacific atmospheric circulation due to anthropogenic forcing. *Nature*, **441**, 73–76.

Vuille, M., and M. Werner, 2005: Stable isotopes in precipitation recording South American summer monsoon and ENSO variability: observations and model results. *Clim. Dyn.*,.

——, ——, R. S. Bradley, R. Y. Chan, and F. Keimig, 2005: Stable isotopes in East African precipitation record Indian Ocean zonal mode. *Geophys. Res. Lett.*, **32**, 2307.

Vystavna, Y., I. Matiatos, and L. I. Wassenaar, 2020: 60-year trends of δ18O in global precipitation reveal large scale hydroclimatic variations. *Glob. Planet. Change*, **195**, 103335.

Walker, G. T., and E. W. Bliss, 1932: World Weather V. *Memoirs of the Royal Meteorological Society*, **4**, 53–84.

——, and ——, 1937: World Weather VI. *Memoirs of the Royal Meteorological Society*, **4**, 119–139.

Watanabe, M., H. Shiogama, H. Tatebe, M. Hayashi, M. Ishii, and M. Kimoto, 2014: Contribution of natural decadal variability to global warming acceleration and hiatus. *Nat. Clim. Chang.*, **4**, 893–897.

Wolf, A., W. H. G. Roberts, V. Ersek, K. R. Johnson, and M. L. Griffiths, 2020: Rainwater isotopes in central Vietnam controlled by two oceanic moisture sources and rainout effects. *Sci. Rep.*, **10**, 16482.

Wu, A., and W. W. Hsieh, 2004: The nonlinear association between ENSO and the Euro-Atlantic winter sea level pressure. *Climate Dynamics*, **23**, 859–868, https://doi.org/10.1007/s00382-004-0470-5.

Xie, P., and P. A. Arkin, 1997: Global Precipitation: A 17-Year Monthly Analysis Based on Gauge Observations, Satellite Estimates, and Numerical Model Outputs. *Bull. Am. Meteorol. Soc.*, **78**, 2539–2558.

Yim, B. Y., S.-W. Yeh, H.-J. Song, D. Dommenget, and B. J. Sohn, 2017: Land-sea thermal contrast determines the trend of Walker circulation simulated in atmospheric general circulation models. *Geophys. Res. Lett.*, **44**, 5854–5862.

Yu, L., S. A. Josey, F. M. Bingham, and T. Lee, 2020: Intensification of the global water cycle and evidence from ocean salinity: a synthesis review. *Ann. N. Y. Acad. Sci.*, **1472**, 76–94.

Zhang, W., T. Zhou, L. Zhang, and L. Zou, 2019: Future Intensification of the Water Cycle with an Enhanced Annual Cycle over Global Land Monsoon Regions. *J. Clim.*, **32**, 5437–5452.

Zwart, C., N. C. Munksgaard, N. Kurita, and M. I. Bird, 2016: Stable isotopic signature of Australian monsoon controlled by regional convection. *Quaternary Science Reviews*, **151**, 228–235, https://doi.org/10.1016/j.quascirev.2016.09.010.

Figures

Figure 1

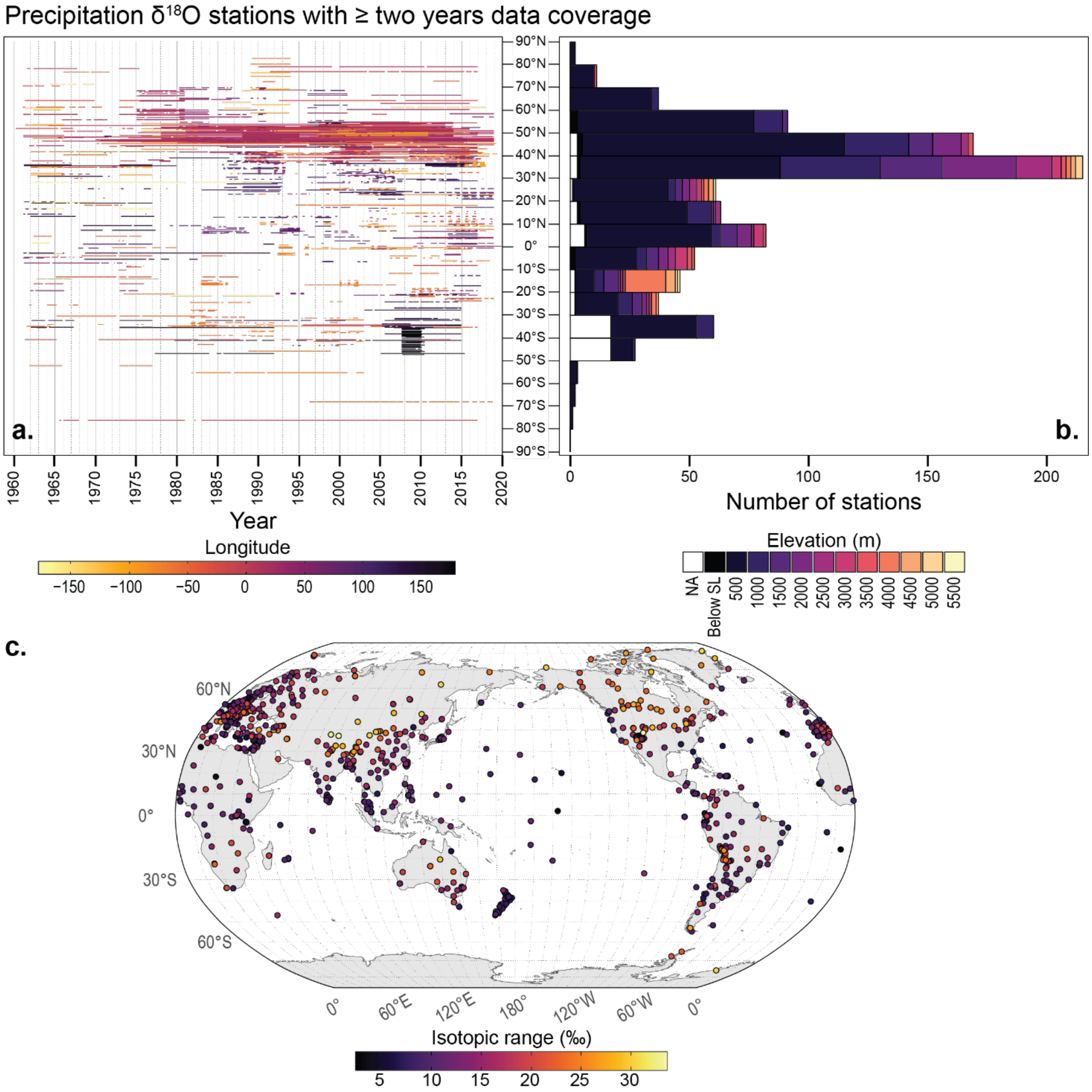

Figure 1. Spatial and temporal distribution of monthly δ18OP observations at stations with at least two years of data coverage. Panel **a)** shows the temporal availability from each station, arranged by station latitude and coloured by station longitude. Panel **b)** shows the total number of stations in each 10° latitudinal bin, separated by station elevation. Panel **c)** shows the global distribution of stations, coloured by the total range in δ18OP values recorded at each station.

Figure 2

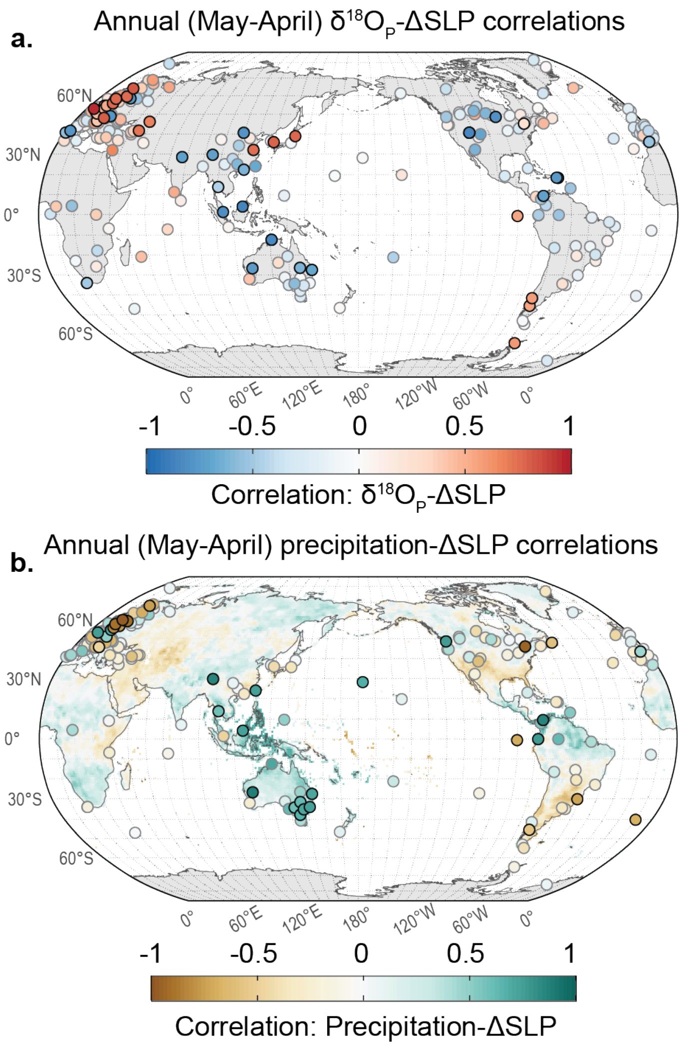

Figure 2. Pearson correlation coefficients showing the strength and direction of the relationship between **a)** precipitation-weighted annual-mean $\delta^{18}O_P$ values and ΔSLP and **b)** annual-mean precipitation and ΔSLP. In all cases, annual means are calculated from May-April. Panel **a)** only includes sites with five or more years of data coverage. Panel **b)** shows correlations for the full GPCC precipitation field (1960-2016; shading), as well as precipitation subsampled to exactly match the spatial and temporal resolution of the $\delta^{18}O_P$ station data (points). A black border around a point denotes a significant correlation ($p < 0.05$).

Figure 3

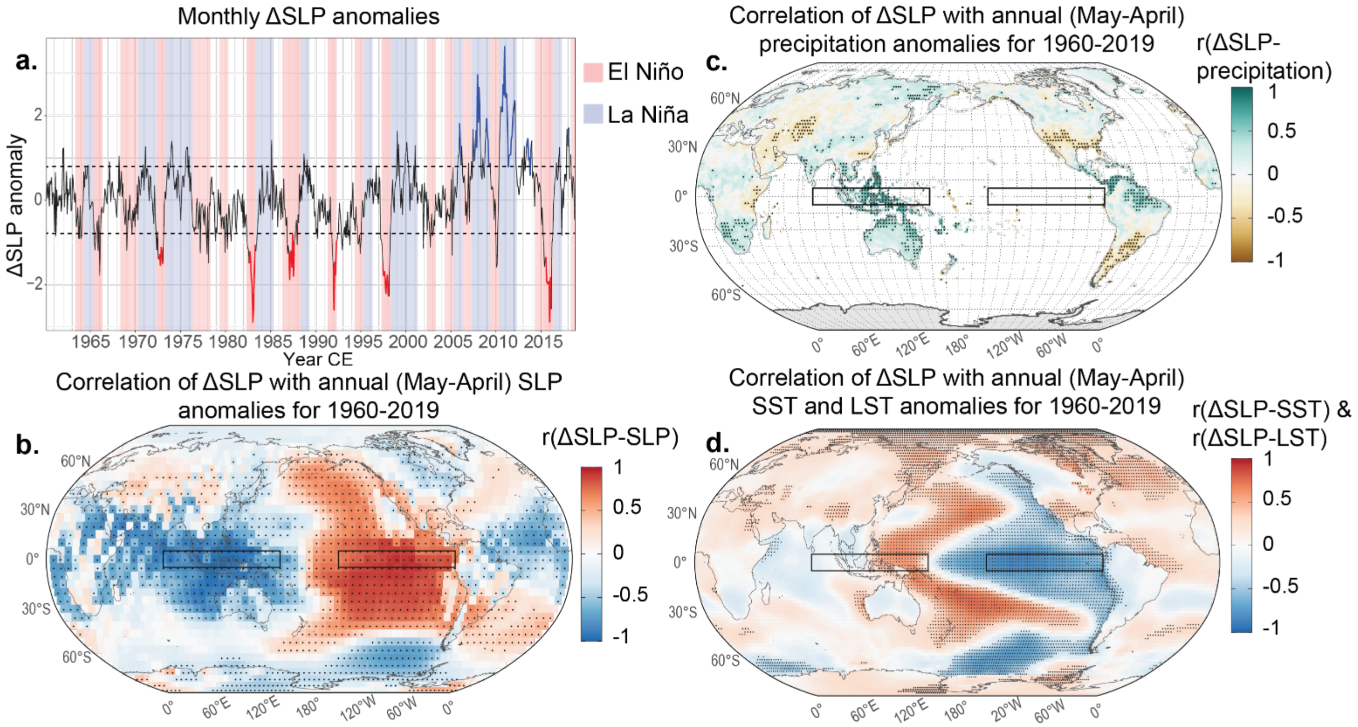

Figure 3. a) Monthly anomalies in the equatorial Indo-Pacific SLP gradient (ΔSLP), calculated as described in **Section 2.4.1**, from 1960 (the first year in which we have $\delta^{18}O_P$ data). Blue (red) lines denote years with anomalously positive (negative) ΔSLP (defined as per **Section 2.7.1**). Dashed black line shows one standard deviation in ΔSLP. Red and blue windows denote El Niño and La Niña years, respectively (defined as per **Section 2.7.1).** Correlation of annual-mean **b)** SLP, **c)** terrestrial precipitation, **d)** land and sea surface temperature (LST & SST) anomalies with annual-mean ΔSLP, for 1960-2019 (tropical years). Boxes on the three maps show the regions used to calculate the ΔSLP index. Stippling denotes a significant correlation ($p < 0.05$), controlling for false discovery rate (FDR; Benjamini and Hochberg 1995).

Figure 4

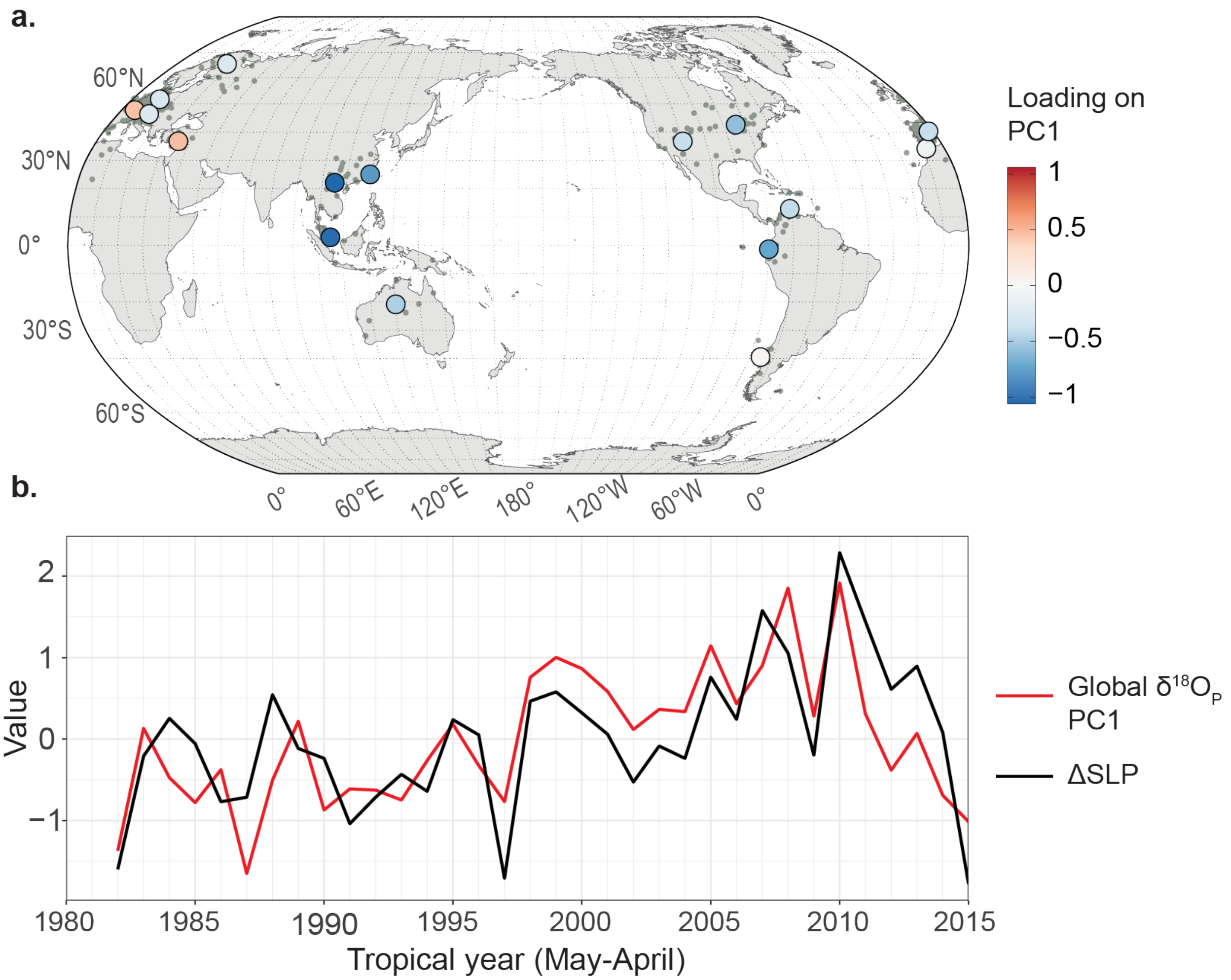

Figure 4. a) Larger points show the leading empirical orthogonal function from the 16 long regional $\delta^{18}O_P$ composites (global $\delta^{18}O_P$ EOF1), i.e., the spatial loadings on the first principal component from the $\delta^{18}O_P$ composites (global $\delta^{18}O_P$ PC1). The smaller grey points show individual sites that contributed to the 16 regional composites. The red line in panel **b)** shows global $\delta^{18}O_P$ PC1, i.e., the time series associated with global $\delta^{18}O_P$ EOF1. Global $\delta^{18}O_P$ PC1 explains 56 % of the total variance in the dataset. The black line in panel **b)** shows annual-mean (May-April) ΔSLP. The correlation between global $\delta^{18}O_P$ PC1 and ΔSLP over this interval is 0.74 i.e. ΔSLP explains 55 % of the variance in global $\delta^{18}O_P$ PC1 ($p < 0.05$).

Figure 5

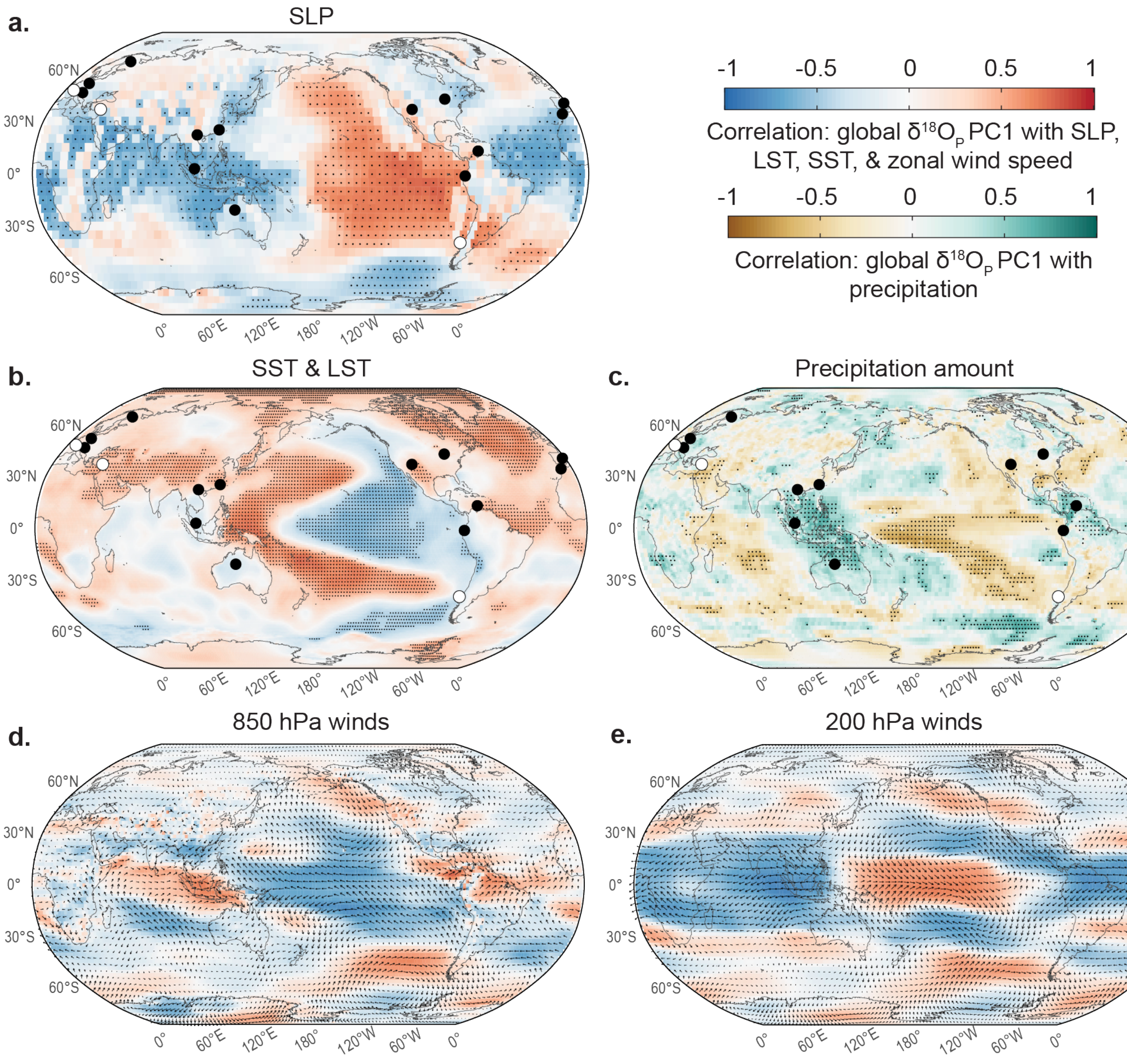

Figure 5. Pearson correlation coefficients showing the strength and direction of the relationship between global δ^{18}O$_P$ PC1 and annual-mean (May-April) anomalies in **a)** SLP, **b)** surface temperature, **c)** precipitation, **d)** 850 hPa winds, and **e)** 200 hPa winds, for 1982-2015 (tropical years). Points in panels **a-c** show the location of the regional composites whose variability is summarised by global δ^{18}O$_P$ PC1; a black circle denotes a negative loading on global δ^{18}O$_P$ PC1 (i.e., blue-coloured points in **Fig. 4a**) and a white circle denotes a positive loading on global δ^{18}O$_P$ PC1 (i.e., red-coloured points in **Fig. 4a**). Stippling denotes a significant correlation ($p < 0.05$), controlling for FDR (Benjamini and Hochberg 1995).

Figure 6

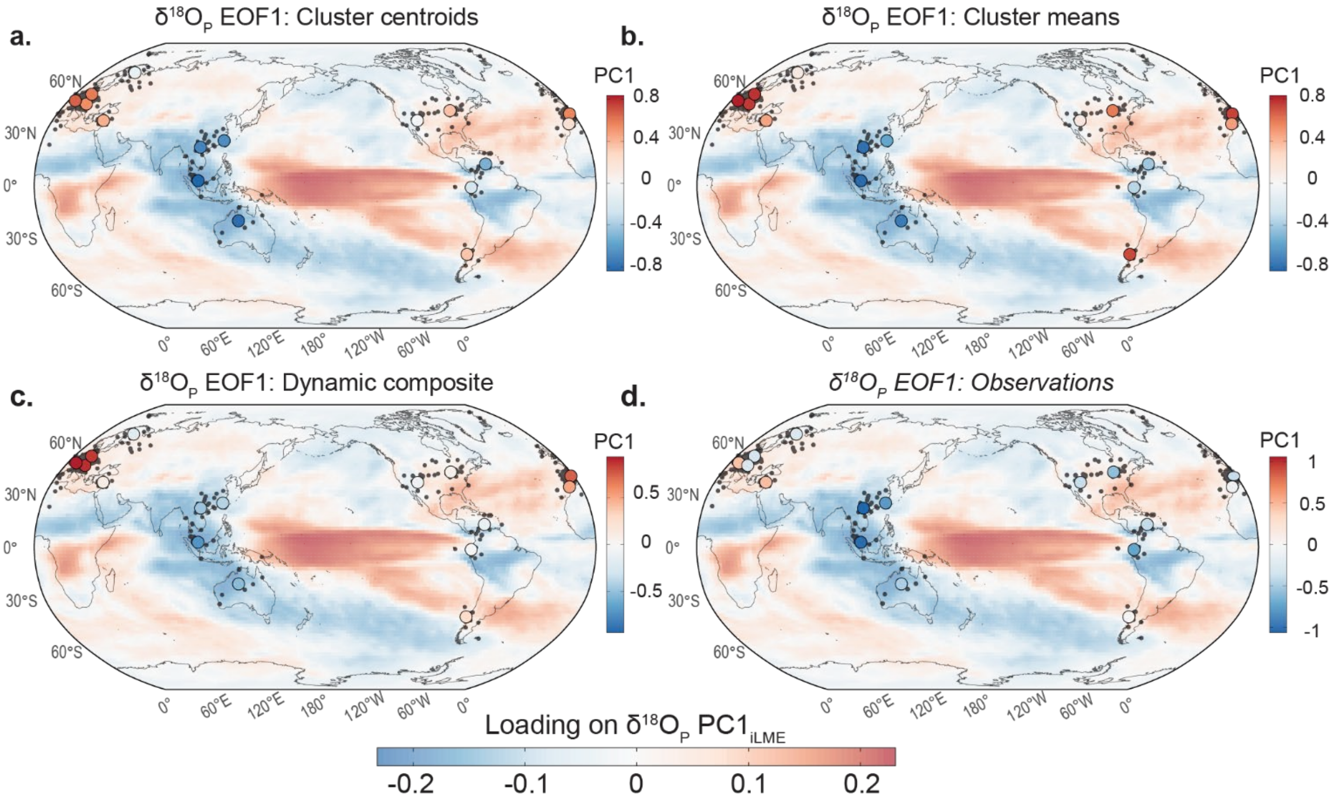

Figure 6. a-c) The leading $\delta^{18}O_P$ empirical orthogonal function (EOF1) for the three iLME *subsets* (large points; calculated as described in **Section 2.9**), superimposed on EOF1 of the *full* iLME $\delta^{18}O_P$ field ($\delta^{18}O_P$ EOF1$_{iLME}$). Smaller grey points show the location of grid cells contributing to the iLME subsets (equivalent to site locations shown in **Fig. 4a**). For ease of comparison, panel **d)** shows global $\delta^{18}O_P$ EOF1 from the observational data (**Fig. 4a**), similarly superimposed on $\delta^{18}O_P$ EOF1$_{iLME}$. Scale bars adjacent to each map correspond to the points, showing the loading of each subset on the associated PC1. The scale bar below the four panels corresponds to $\delta^{18}O_P$ EOF1$_{iLME}$. The titles above each map refer to the EOF point markers superimposed on $\delta^{18}O_P$ EOF1$_{iLME}$. All maps show the mean of the three full-forcing simulations.

Figure 7

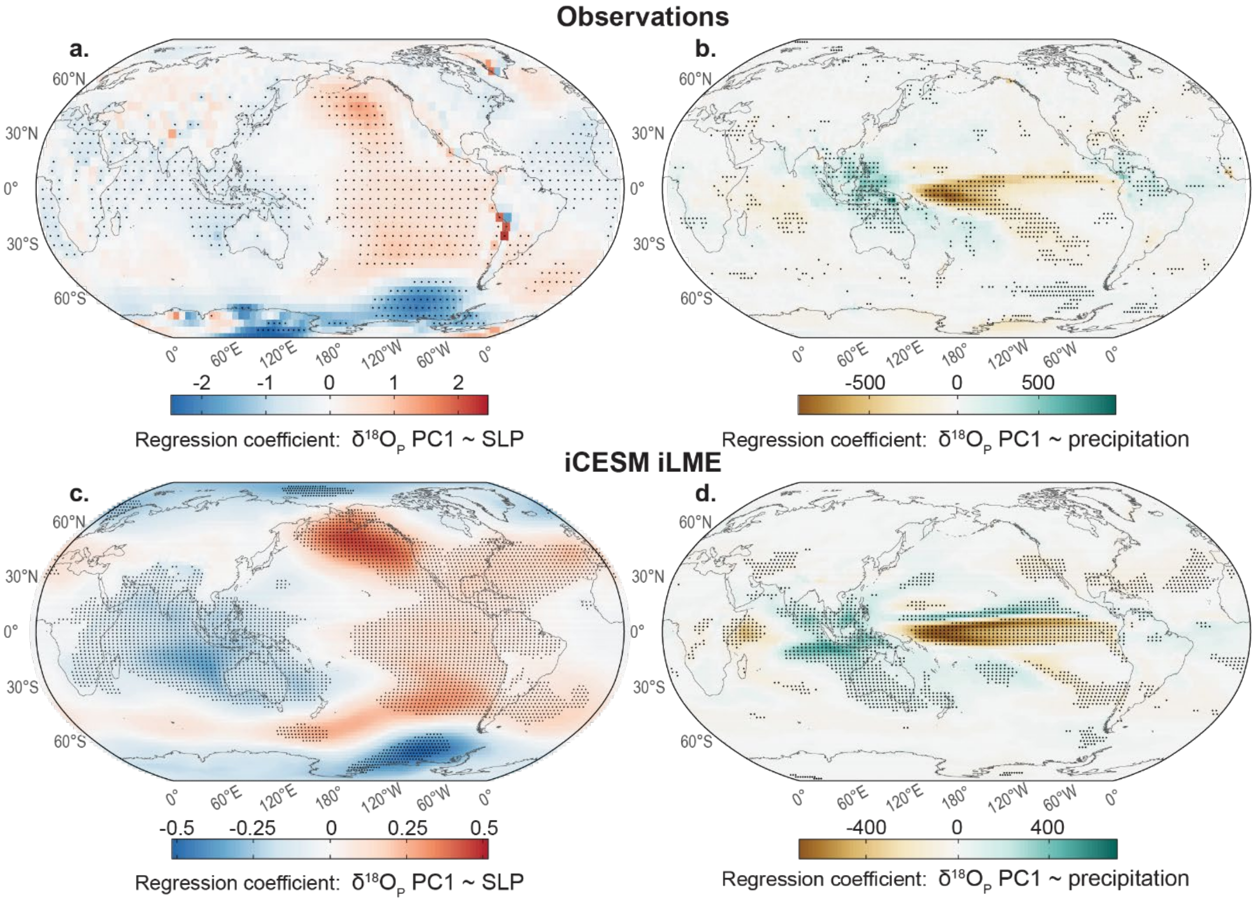

Figure 7. Regression coefficients showing the structure and direction of the relationship between $\delta^{18}O_P$ PC1 and climatic variables in observations (**a, b**) and within iCESM (**c, d**). $\delta^{18}O_P$ PC1 from observations is global $\delta^{18}O_P$ PC1 as described in the main text (**Fig. 4b**), and $\delta^{18}O_P$ PC1 from the iLME is $\delta^{18}O_P$ $PC1_{iLME}$ as described in the main text, i.e., the first PC of the full iLME $\delta^{18}O_P$ fields. Panels **a)** and **c)** show the regression of $\delta^{18}O_P$ PC1 on annual-mean SLP, and panels **b)** and **d)** show the regression of $\delta^{18}O_P$ PC1 on annual-mean precipitation amount. Stippling denotes a significant relationship ($p < 0.05$), controlling for FDR (Benjamini and Hochberg 1995).

Tables

Table 1

Tropical Pacific atmospheric variability	**PWC (ΔSLP)**	**SOI**	**PWC (u winds)**
	0.74*	0.7*	-0.64*
	(0.43*)	(0.39*)	(-0.29)
Tropical Pacific oceanic variability	**Niño 3.4**	**EMI**	
	-0.58*	-0.44*	
	(-0.36*)	(-0.43*)	
Variability outside the tropical Pacific	**PMM**	**SAM**	**DMI**
	-0.33	0.24	-0.03
	(-0.36)	(0.29*)	(0.06*)

Table 1. Pearson correlation coefficients showing the strength and direction of the relationship between global $\delta^{18}O_P$ PC1 and indices for tropical Pacific atmospheric variability (top row), tropical Pacific oceanic variability (middle row) and extra-Pacific or extra-tropical variability (bottom row). For comparison, correlations of each index with the corresponding global *precipitation* PC1 are shown underneath in parentheses. In both cases, an asterisk denotes a significant correlation ($p < 0.05$). PWC = Pacific Walker Circulation, SOI = Southern Oscillation Index, EMI = ENSO Modoki Index, PMM = Pacific Meridional Mode, SAM = Southern Annular Mode, DMI = Dipole Mode Index. All indices are defined in **Section 2.4**.

Table 2

Subset	**Correlation with full field PC1**	**Correlation with ΔSLP**
Full field	1	0.96
Cluster centroids	0.81	0.78
Cluster means	0.8	0.78
Dynamic composite	0.61	0.62
Observations	*NA*	*0.74*

**All correlations significant ($p < 0.05$)*

Table 2. The first column shows the correlation between PC1 of each iLME *subset* and PC1 of the full iLME $\delta^{18}O_P$ field ($\delta^{18}O_P$ $PC1_{iLME}$). The second column shows the correlation of each PC1 with annual-mean (May-April) ΔSLP. All correlation coefficients are the mean of the three full-forcing simulations. For comparison, the equivalent correlation coefficient from the observational data is provided in the last row.

Supplementary Information
Supp. Fig. 1

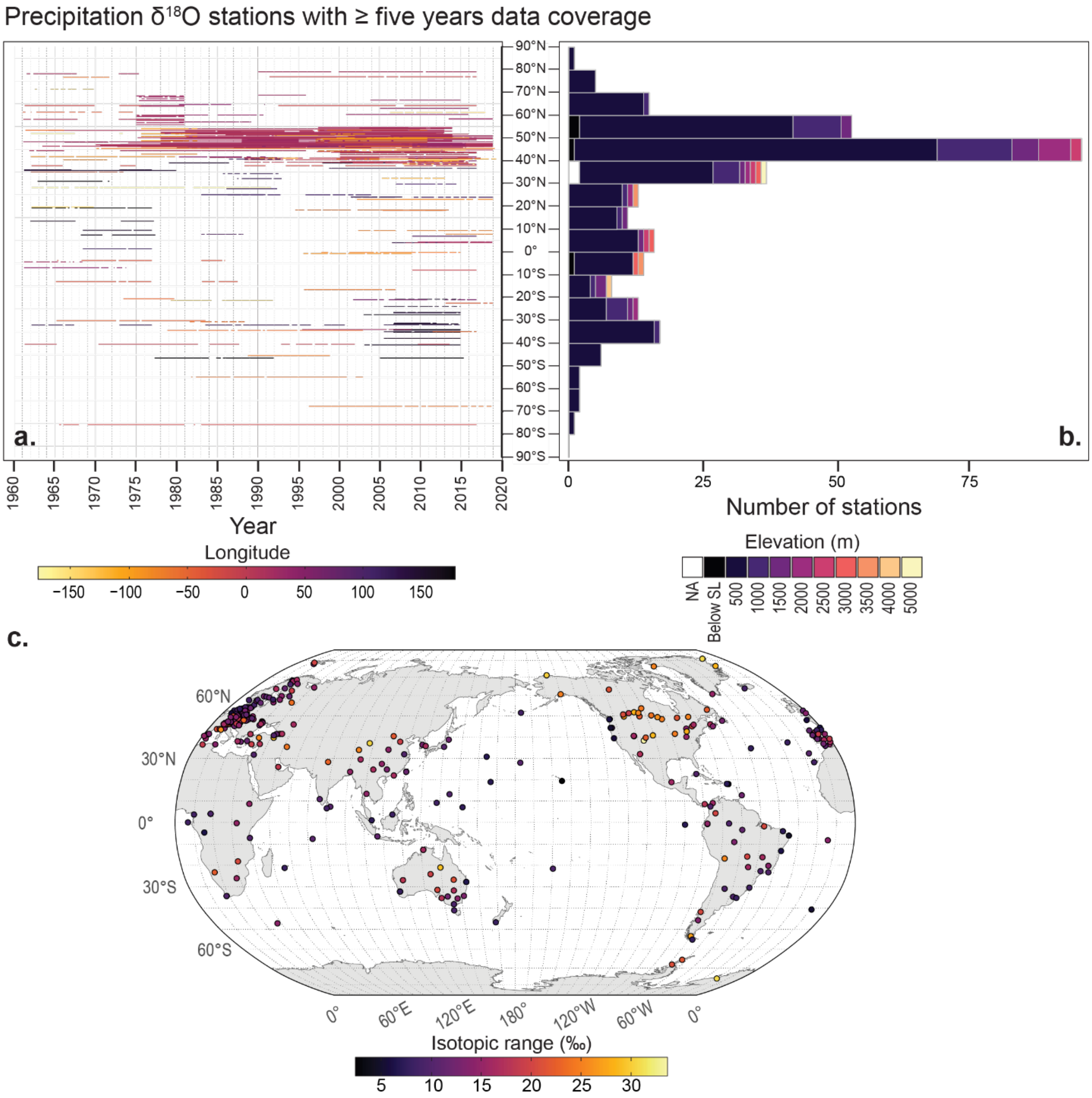

Figure S1. As per main text Fig. 1, but only showing stations with five or more years of data coverage.

Supp. Fig. 2

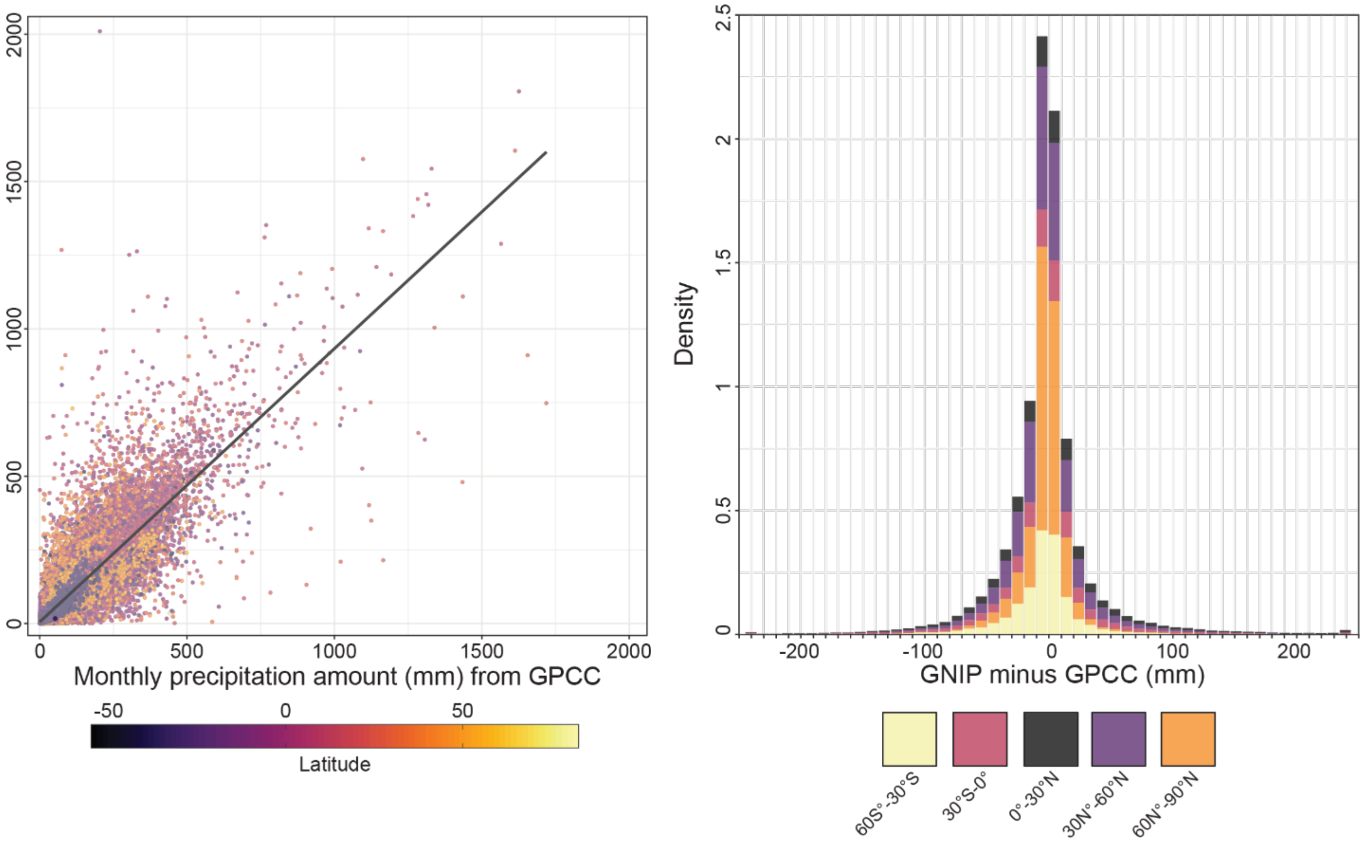

Figure S2. Comparison of monthly precipitation amount data from the Global Precipitation Climatology Centre (GPCC) gridded observational product (Becker et al. 2013), and precipitation observations included in the Global Network of Isotopes in Precipitation database (GNIP) (IAEA/WMO 2020). Panel **a)** shows an equal-axis cross-plot of precipitation amount observations recorded in the GNIP database compared with data from the same months from the equivalent grid cells in GPCC. Points are coloured by station latitude. Panel **b)** shows the distribution of offsets between monthly precipitation as recorded in GPCC versus GNIP. Distributions are split into 30° latitudinal bands. Note that GPCC does not cover Antarctica.

Supp. Fig. 3

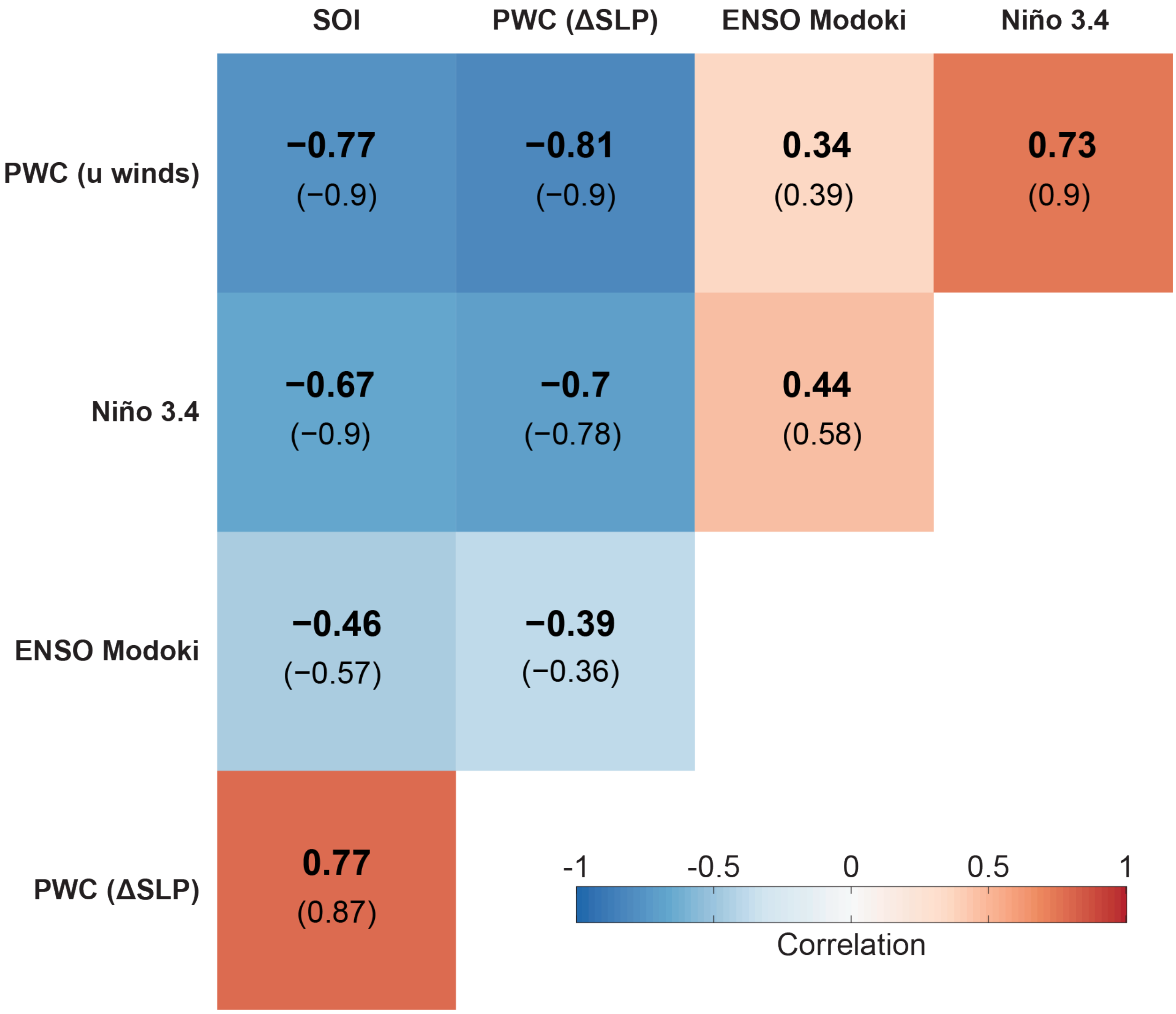

	SOI	PWC (ΔSLP)	ENSO Modoki	Niño 3.4
PWC (u winds)	**−0.77** (−0.9)	**−0.81** (−0.9)	**0.34** (0.39)	**0.73** (0.9)
Niño 3.4	**−0.67** (−0.9)	**−0.7** (−0.78)	**0.44** (0.58)	
ENSO Modoki	**−0.46** (−0.57)	**−0.39** (−0.36)		
PWC (ΔSLP)	**0.77** (0.87)			

Figure S3. Correlation matrix showing the strength and direction of the relationship between various indices for tropical Pacific variability, for the full interval covered by all indices i.e. 1981-2018. Colours correspond to the monthly correlations, which are also shown in bold text. Equivalent annual correlations are shown in parentheses. Squares are ordered by hierarchical clustering.

Supp. Fig. 4

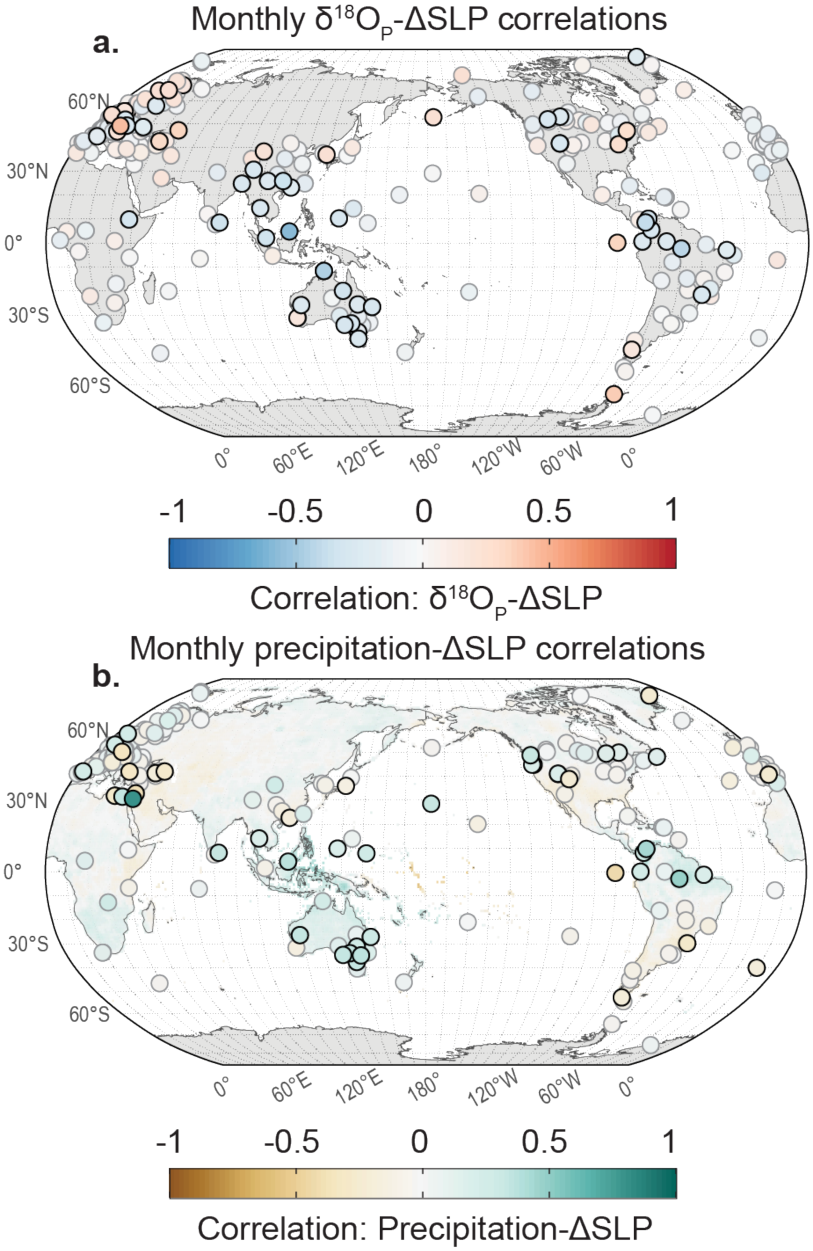

Figure S4. All as per main text **Fig. 2**, but showing monthly correlations rather than annual.

Supp. Fig. 5

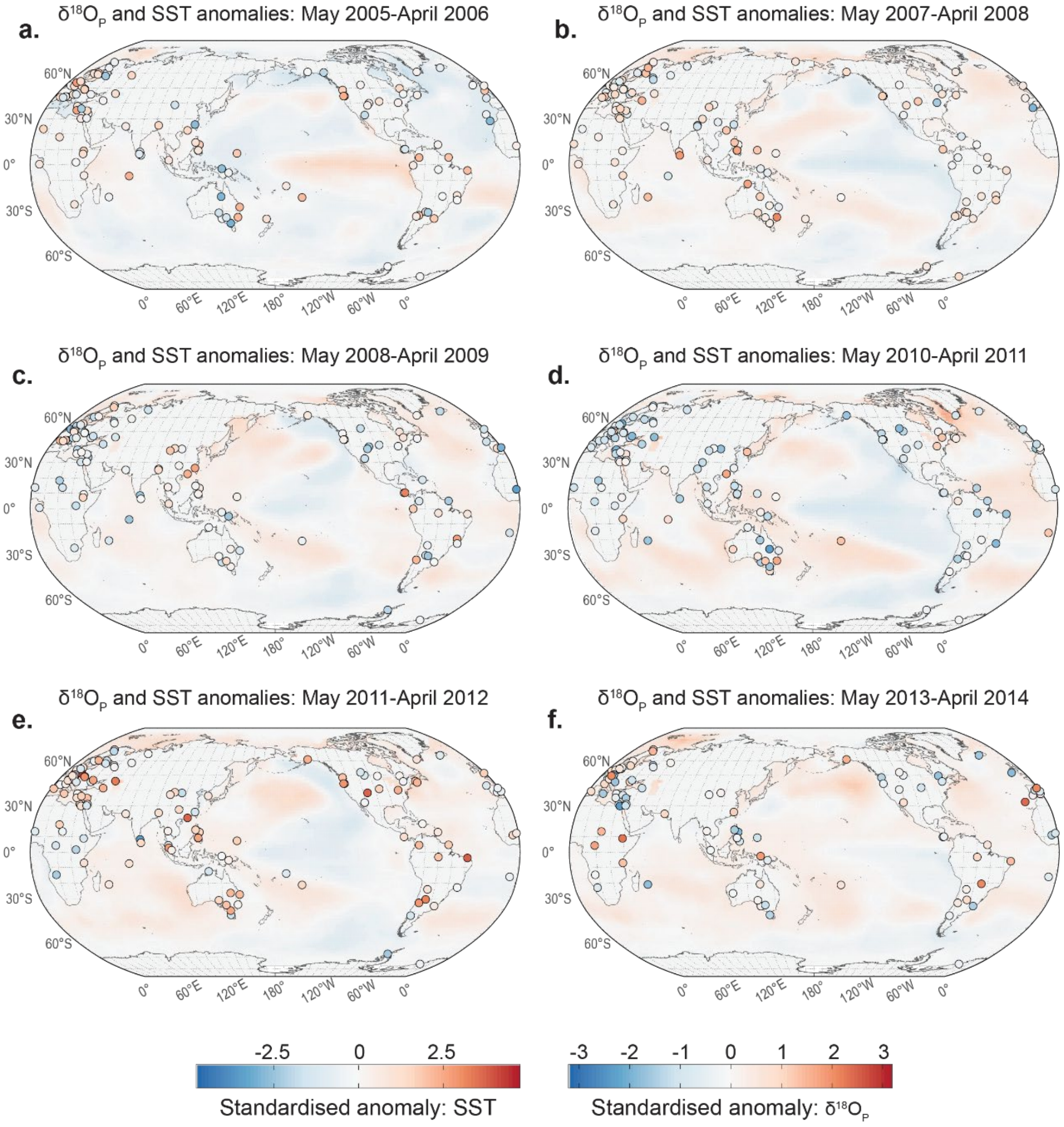

Figure S5. $\delta^{18}O_P$ and SST standardised anomaly ('z-score') maps for years with anomalously *strong* PWC, as defined by years in which a three-month moving average of the monthly ΔSLP index exceeds one standard deviation above the mean, for five or more consecutive months (**Fig. 3a, Section 2.7.1**). Points show all sites that have at least five years of $\delta^{18}O_P$ observations **and** have $\delta^{18}O_P$ observations in the year of interest. Years are 'tropical years' i.e. starting in May of calendar year one and finishing in April of calendar year two. $\delta^{18}O_P$ anomalies are relative to the mean of the full record. SST anomalies are relative to the 1960-2019 mean.

Supp. Fig. 6

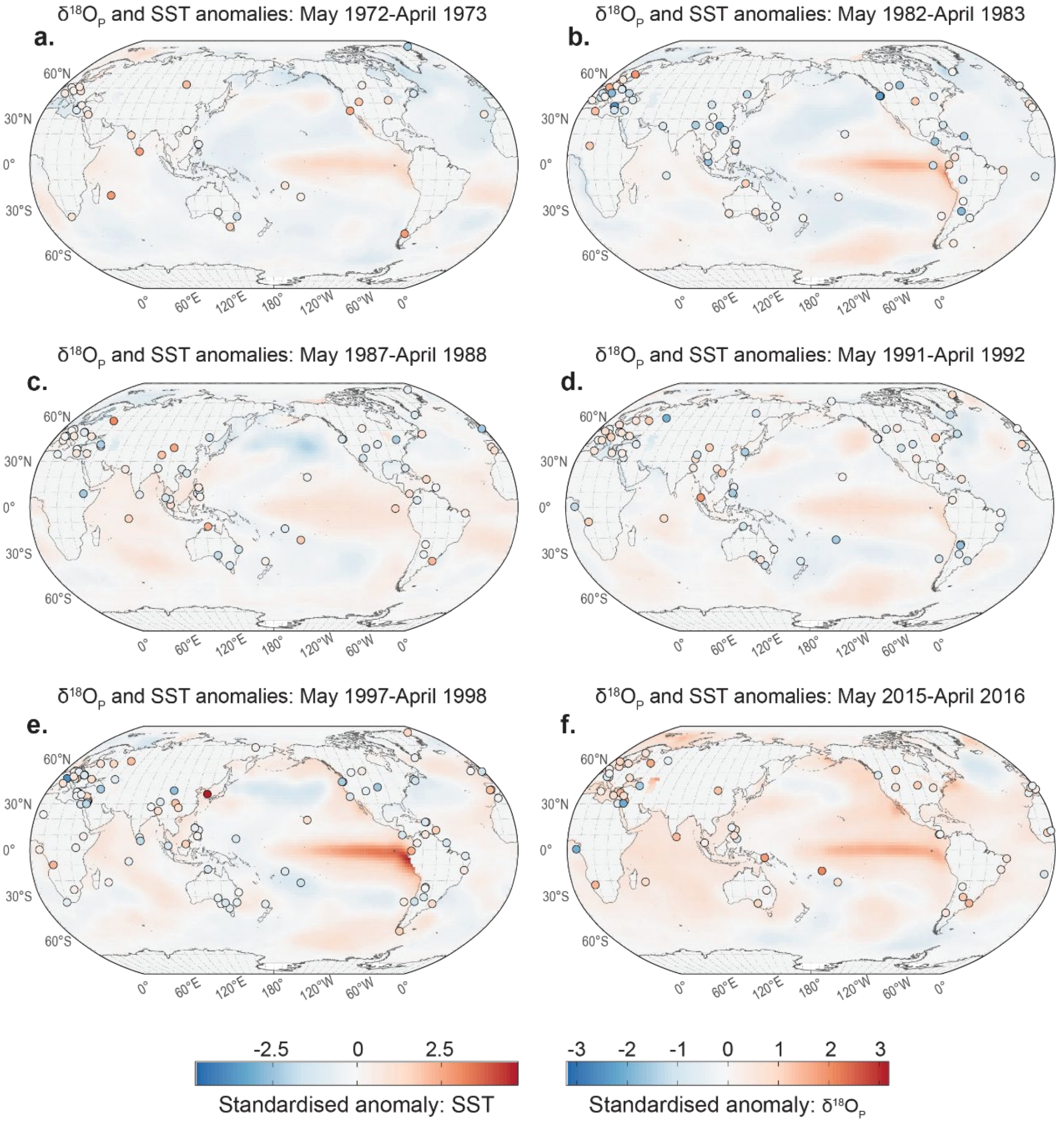

Figure S6. As per **Supp. Fig. 5** but for years with anomalously *weak* PWC, as defined by years in which a three-month moving average of the monthly ΔSLP index exceeds one standard deviation below the mean, for five or more consecutive months (**Fig. 3a, Section 2.7.1**).

Supp. Fig. 7

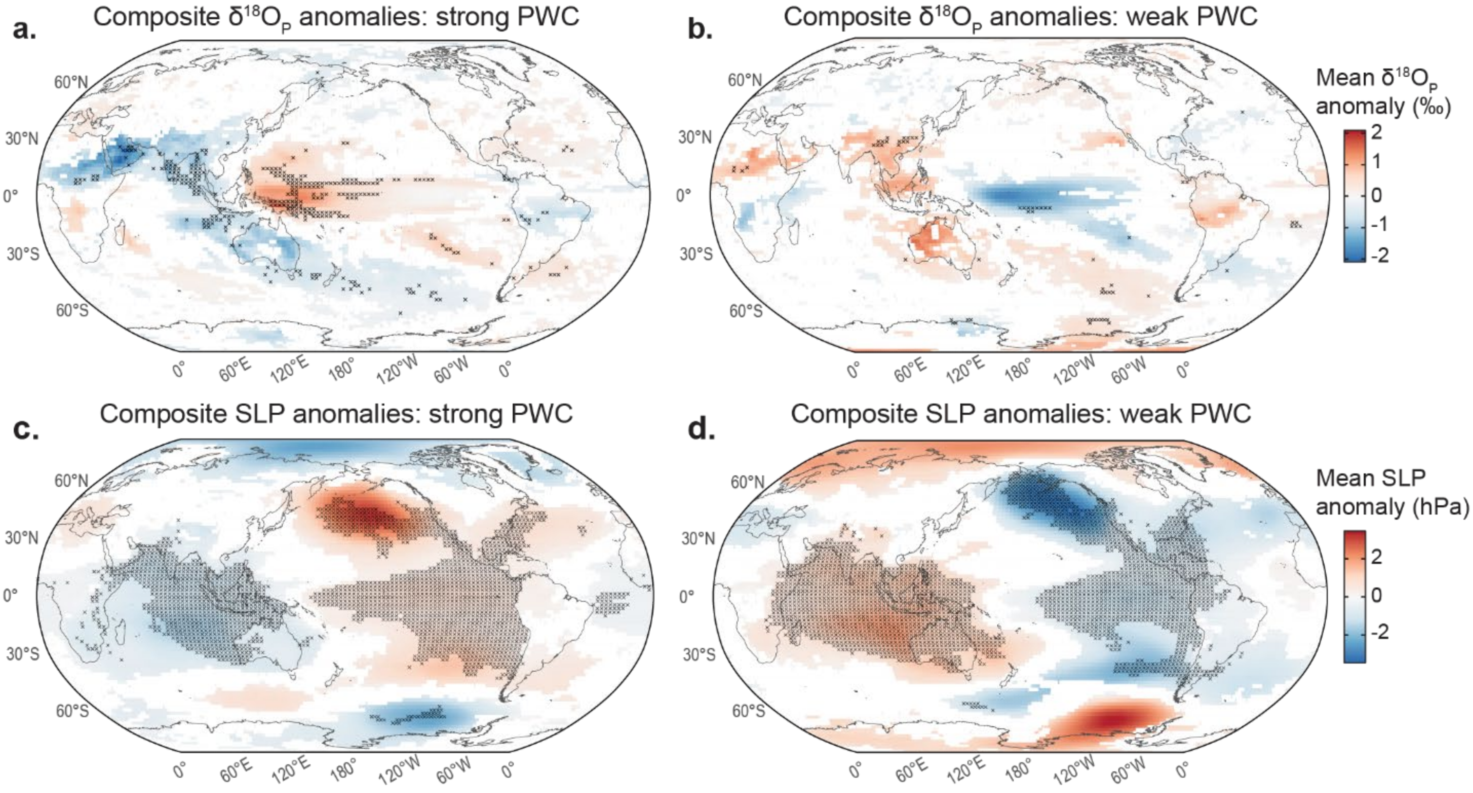

Figure S7. a) and **c)** show δ^{18}O$_P$ and SLP composite anomaly maps for years with anomalously *strong* PWC (anomalously positive ΔSLP) defined as per **Fig. S5**. δ^{18}O$_P$ and SLP anomalies are the mean of all 'high ΔSLP' years from the iLME three full-forcing ensemble members (n = 19 years). Stippling denotes ≥90 % agreement on the sign of the anomaly in years with anomalously high ΔSLP. White-shaded cells denote <66 % agreement on the sign of the anomaly. Note that 50 % agreement indicates essentially no agreement on the sign of the anomaly. Panels **b & d)** are as per **a & c)** but showing the composite anomalies for years of *weak* PWC (anomalously negative ΔSLP), defined as per **Fig. S6** (n = 26). Years are 'tropical years' i.e. starting in May of calendar year one and finishing in April of calendar year two. δ^{18}O$_P$ and SLP anomalies are relative to the 1960-2005 mean for that grid cell.

Supp. Fig. 8

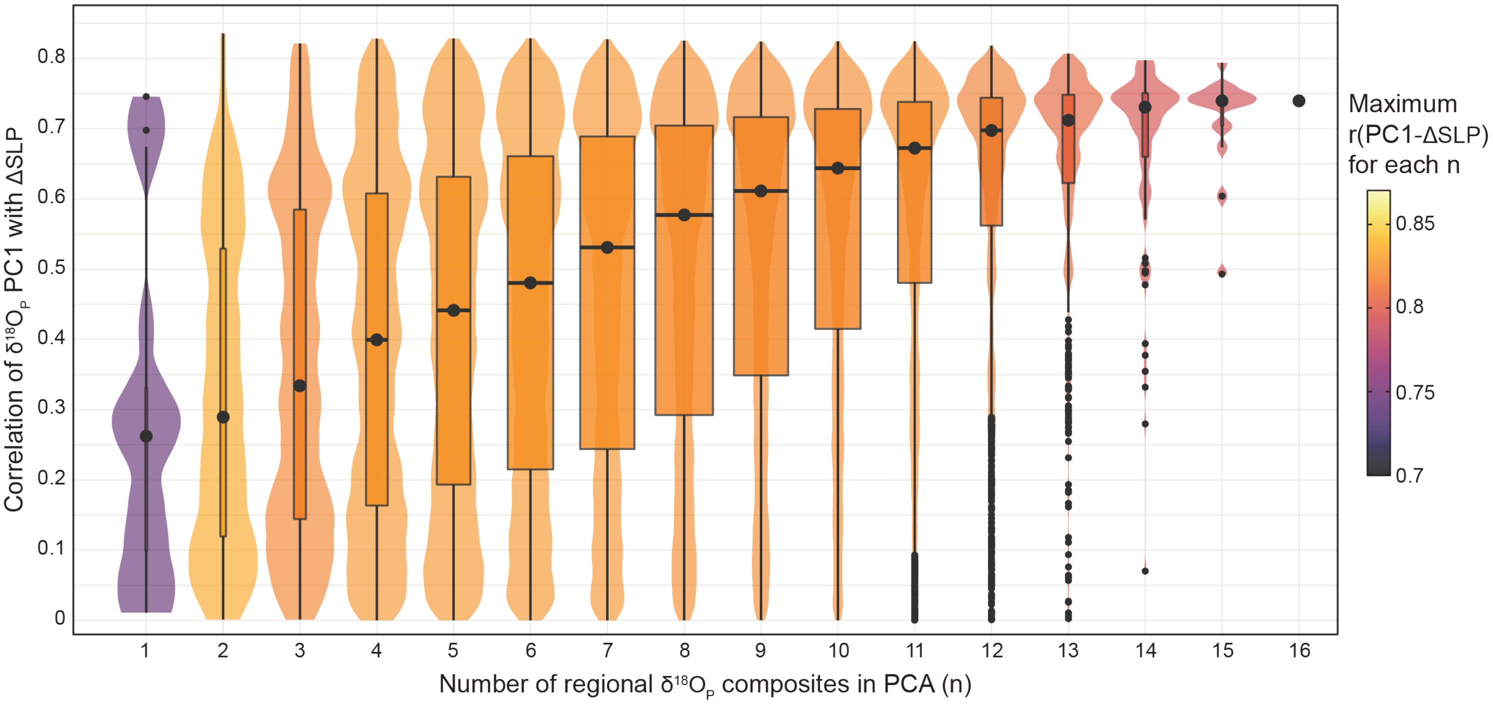

Figure S8. Violin-and-boxplots ('voxplots') showing the correlations of ΔSLP with the first principal component of variability (PC1) of all possible combinations of the 16 regional $\delta^{18}O_P$ composites (described in **Section 2.8.2**), from n = 1 to n = 16. Black dots for each n show the median correlation; voxplots are coloured according to the maximum PC1~ΔSLP correlation for that n. The width of the boxes scales with the total number of possible site combinations (maximum of 12870). Underlying violin plots show the distribution of correlations for each n. In the case of n = 1, the correlations are simply those of the individual $\delta^{18}O_P$ composites with ΔSLP.

Supp. Fig. 9

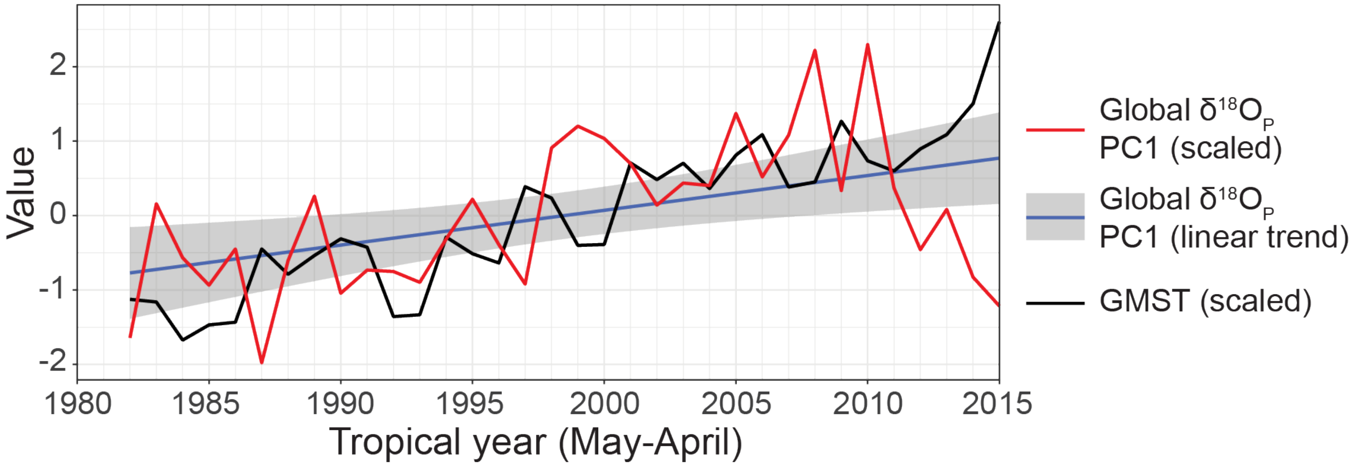

Figure S9. Comparison of global $\delta^{18}O_P$ PC1 with global mean surface temperature (GMST) (Lenssen et al. 2019; GISTEMP Team 2020). Over the analysis interval (1982-2015), a linear regression model suggests that GMST can explain 9 % of the variance in global $\delta^{18}O_P$ PC1, although GMST is not significantly correlated with global $\delta^{18}O_P$ PC1 at the 95 % confidence level ($p = 0.09$). Over the full analysis interval, the linear trend in global $\delta^{18}O_P$ PC1 explains 22 % of the variability in the data ($p < 0.05$). The trend is shown by the blue line, with the 95 % confidence interval in grey. Both timeseries have been scaled by their standard deviation, for easier visual comparison.